# STRUCTURED COHERENCE BEAMS

by

Wenrui Miao

A dissertation submitted to the faculty of
The University of North Carolina at Charlotte
in partial fulfillment of the requirements
for the degree of Doctor of Philosophy in
Optical Science and Engineering

Charlotte

2024

Approved by:

_____
Dr. Greg J. Gbur

_____
Dr. Glenn Boreman

_____
Dr. Michael Fiddy

_____
Dr. William Brian

# ABSTRACT

WENRUI MIAO. Structured coherence beams. (Under the direction of DR. GREG J. GBUR)

This thesis explores advanced manipulation and control of light's structure, focusing on the degrees of freedom such as phase, polarization, and coherence. The research primarily addresses the generation, propagation, and application of structured optical beams, with significant implications for imaging, communication, particle manipulation, microscopy, and quantum state engineering.

A key area of investigation is the use of orbital angular momentum (OAM) in optical beams. These beams, characterized by a conserved topological charge, have shown promise in free-space optical communication due to their resilience against amplitude and phase disturbances. The research highlights the development of partially coherent beams that maintain deterministic vortices at specific propagation distances, achieved through fractional Fourier transforms (FracFTs) applied to Schell-model vortex beams in the source plane.

Another significant focus is on polarization singularities in fields with two harmonic frequencies, i.e. Lissajous singularities. The study reveals stable Lissajous singularities within the beam core, offering new opportunities in high-precision metrology and secure communication. Additionally, Young's interference experiment with bichromatic vector beams is simulated creating Lissajous-type polarization singularities, enhancing the fundamental understanding of the conditions under which Lissajous singularities can be created in interference.

This work integrates these findings into a comprehensive framework for structured coherence beams, advancing theoretical models and experimental techniques. The resulting beams demonstrate unprecedented control over intensity, phase, coherence, and polarization, paving the way for innovative applications in optical science and

engineering.

# DEDICATION

To my elder brother, Wentao Miao.

You have always been a source of pride and inspiration.

We will forever love you.

# ACKNOWLEDGEMENTS

I would like to express my sincere gratitude to my PhD advisor, Dr. Greg J. Gbur, for his unwavering guidance and support throughout the entirety of my five-year doctoral journey. His exemplary role as an advisor and scientist has been a constant source of inspiration.

I extend my thanks to my graduate committee members, Dr. Boreman, Dr. Fiddy and Dr. Brian, for their crucial support at significant milestones in my PhD program.

Special appreciation goes to Dr. Taco D. Visser and Dr. Yongtao Zhang for their meaningful discussions and great assistance with my projects.

I acknowledge financial support from the Air Force Office of Scientific Research (FA9550-21-1-0171), the Office of Naval Research (N00014-20-1-2558), and GASP grants.

Special thanks to my parents Mr. Hekun Miao and Mrs. Yunxia Dong for their generous assistance.

TABLE OF CONTENTS

# LIST OF FIGURES

# LIST OF ABBREVIATIONS

CSD Cross-Spectral Density

DoF Degree of Freedom

DVB Deterministic Vortex Beam

FracFTs Fractional Fourier Transforms

GSMV Gaussian Schell-Model Vortex

LG Laguerre–Gauss

OAM Orbital Angular Momentum

SHG Second Harmonic Generation

# PREFACE

The manipulation and control of light's structure has ushered in a new era of optical science, enabling groundbreaking applications across various fields such as imaging, communication, particle manipulation, microscopy, and quantum state engineering[1]. Light can be tailored in all of its degree of freedoms(DoFs), from amplitude, phase, polarization to coherence. This thesis aims to investigate the generation, propagation and application of these optical beams with sophisticated and novel structures.

Though the richness of studies of structured beams and its myriad applications recently have drawn attention to the manipulation of many different DoFs, in the beginning, structured beams are almost synonymous with beams containing orbital angular momentum(OAM). In a monochromatic field, beams with OAM possess a topological charge which is always an integer because the phase change by multiples of $2\pi$ along closed paths around the vortex core. The topological charge is conserved and resilient to amplitude and phase disturbances in the field. Due to their discrete and robust properties, many researches have investigated the use of optical vortices as information carriers in free space optical communication systems[2]. Because different vortex modes are orthogonal to one another, it is theoretically possible to transmit information using multiple vortex orders simultaneously through the same channel, thereby significantly increasing data transmission rates[3]. The conservation of topological charge also suggests robustness against atmospheric turbulence. However, such turbulence can still impair system performance by causing the vortex to drift out of the detector area or by creating additional vortex pairs through self-interference. However, it has been found that fields with a reduced spatial coherence, i.e. partially coherent fields show higher levels of resistance to turbulence compared to its coherent counterparts[4]. Because partially coherent beams reduce the self-interference effects, the strength of intensity fluctuations is reduced accordingly[5]. However, traditionally, the deterministic phase structure of optical vortices was seen

as incompatible with the random phase fluctuations inherent in partially coherent fields[6]. A deterministic vortex imparted on a partially coherent field, through the use of a spiral phase plate, for example, would appear to always transform into a coherence vortex on propagation; similarly, if a random phase is imparted on a deterministic vortex beam (DVB), that vortex will also transform into a coherence vortex on propagation[7]. In our research, we have demonstrated that it is possible to design partially coherent beams that manifest a deterministic vortex at any desired propagation distance in free space by implementing fractional Fourier transforms(FracFTs) on a Schell-model vortex beams in the source plane. Such beams hold promise for applications in optical manipulation, where precise control over beam shape and coherence is essential, as well as in remote sensing and free-space optical communication, where resilience to environmental perturbations is crucial[8].

In addition to phase and coherence, another important degree of freedom of light the thesis investigated is polarization. In the simplest case, the polarization across the transverse profile of a paraxially propagating light beam is homogeneous. However, it can also exhibit a spatially inhomogeneous and complex distribution. With the development of both near-field microscopy[9] and particle-based nanointerferometry[10], the measurement of the full field polarization information at the nanoscale, polarization structured light has allowed for a wide range of applications in optical communications, microscopy and many other fields of optics[11]. Typical polarization singularities are lines along which the state of polarization is circular, with the major axis of the polarization ellipse indeterminate. These singularities have been employed in various applications, including imaging, particle trapping and rotation, and free-space communications. Most investigations in the field of polarization singularities have concentrated on monochromatic or quasi-monochromatic fields. However, in 2003, Kessler and Freund[12] identified a novel class of singularities applicable to fields with two harmonic frequencies: a fundamental frequency $\omega$ and its first har-

monic $2\omega$. In this context, the singularities manifest as lines in three-dimensional space where the generalized orientation of the polarization figure, now represented as a Lissajous figure, becomes indeterminate. In our study, we have revealed that the on-axis Lissajous singularity in the beam core of the designed Lissajous beams can be stable and propagate over significant distances. The ability to generate and control these singularities opens new possibilities for their application in high-precision metrology, advanced imaging systems, and secure communication channels.

The exploration of Lissajous singularities was further extended through Young's interference experiment[13], which provided a platform to observe the interference of bichromatic vector beams. This study elucidated the conditions necessary for the formation of Lissajous-type polarization singularities on an observation screen[14], highlighting the intricate relationship between polarization and interference. By manipulating the polarization properties of the incident beams, it is possible to engineer specific polarization interference patterns that can be used in optical metrology and polarization-based imaging techniques.

This thesis seeks to synthesize these advancements into a comprehensive framework for structured coherence beams. By combining the design of Lissajous beams, interference-induced Lissajous patterns, and deterministic vortices in partially coherent fields, we aim to develop new theoretical models and experimental techniques for generating and manipulating structured light. The resulting beams are expected to exhibit unprecedented control over intensity, phase, coherence and polarization, paving the way for innovative applications in optical science and engineering.

The subsequent chapters will delve into the theoretical foundations of structured coherence beams, presenting detailed analyses and simulations of their behavior. Experimental methodologies for generating and characterizing these beams will also be discussed, along with potential applications in various technological domains. Through this integrated approach, this thesis aspires to contribute to the advancement of phys-

ical optics and to unlock new capabilities in the manipulation of light.

# CHAPTER 1: DETERMINISTIC VORTICES EVOLVING FROM PARTIALLY COHERENT FIELDS

## 1.1 Introduction

Over the past few decades, research into optical wavefield singularities [15, 16, 17] has become ubiquitous and has led to many interesting physical insights and potential applications, including micromanipulation [18], optical trapping [19], imaging [20] and free-space optical communications [21, 22]. The most common singularity is an optical vortex, a line of zero intensity in a three-dimensional wavefield around which the phase has a circulating or helical structure. It was soon recognized that the handedness of the phase structure imbues a vortex beam with orbital angular momentum, and that such OAM can be used to trap or rotate particles [23], or create light-driven micromachines [24].

Optical coherence theory is another field of optics that has been researched intensely in recent years, with many potential applications[25] such as intensity interferometry [26], ghost imaging [27], and optical coherence tomography [28]. Partially coherent beams can be structured to have unusual propagation characteristics like self-focusing [29], and it is now well-known that partially coherent beams are in many circumstances resistant to the distortions caused by atmospheric turbulence [4]. These observations have motivated the study of partially coherent beams to improve free-space optical communications [30].

The possibilities of optical vortices and partial coherence make it natural to ask whether there is some benefit to combining their effects. However, it has long been believed that there is an intrinsic conflict between vortices and partial coherence. A vortex is a deterministic phase structure in a spatially coherent field, centered on a line of zero intensity, which we will refer to as a deterministic vortex. In a partially coherent field, the phase is non-deterministic: vortices can appear in two-

point coherence functions with one observation point fixed, where they are referred to as coherence vortices, but their position depends on the choice of observation point and is not associated with a zero of intensity. It has been shown that field vortices associated with a zero of intensity are not typically found in a partially coherent field [6]. A deterministic vortex imparted on a partially coherent field, through the use of a spiral phase plate for example, would appear to always transform into a coherence vortex on propagation [7]; similarly, if a random phase is imparted on a deterministic vortex beam, that vortex will also transform into a coherence vortex on propagation.

However, it was recently found that a certain class of partially coherent beams, now called Rankine vortex beams, will evolve a deterministic vortex as they propagate into the far zone [31]. The evolution of a deterministic vortex in a Rankine beam arises because its cross-spectral density (CSD) is the Fourier transform of that of a Gaussian Schell-model vortex beam, with a deterministic vortex at its core, and so the evolution of a Rankine beam to the far zone results in a deterministic vortex embedded in a partially coherent field.

Of most interest for applications such as optical manipulation, remote sensing and free-space optical communications, however, is a partially coherent beam that can be designed to have a deterministic vortex appear at any desired propagation distance. In this letter, we demonstrate that a partially coherent beam can be designed, through the use of FracFTs, to manifest a deterministic vortex at any range and for any degree of spatial coherence in the source plane; we refer to such beams as DVBs. Our analytic results are illustrated with examples, and show that the relationship between phase singularities and partial coherence is more complicated than generally believed.

To characterize the behavior of partially coherent wavefields, we work in the frequency domain and use the CSD function $W(\mathbf{r}_1, \mathbf{r}_2, \omega)$, which may be formally defined as [32]

$$W(\mathbf{r}_1, \mathbf{r}_2, \omega) = \langle U^*(\mathbf{r}_1, \omega) U(\mathbf{r}_2, \omega) \rangle_\omega \tag{1.1}$$

where $\langle \dots \rangle_\omega$ represents the average over an ensemble of monochromatic fields and the asterisk denotes the complex conjugate. For a quasi-monochromatic field, the CSD at central frequency $\omega$ provides an excellent description of the overall behavior of the field, and we suppress $\omega$ as a functional argument for brevity moving forward.

To design a field that creates deterministic vortices at a specified distance, we start with a Gaussian Schell-model vortex (GSMV) beam of the form,

$$W_0(\mathbf{r}_1, \mathbf{r}_2) = \frac{(x_1 - iy_1)(x_2 + iy_2)}{\sigma^2} e^{-r_1^2/2\sigma^2} e^{-r_2^2/2\sigma^2} e^{-|\mathbf{r}_2 - \mathbf{r}_1|^2/2\delta^2}, \tag{1.2}$$

where $\sigma$ represents the waist width of the beam and $\delta$ represents the transverse spatial correlation length. The terms of the form $x+iy$ represent a deterministic vortex, which appears at the origin and has a zero of the spectral density $S(\mathbf{r}) = W(\mathbf{r}, \mathbf{r})$. This function is of Schell-model form because the spectral degree of coherence depends only upon the difference variable, i.e.

$$\mu_0(\mathbf{r}_2 - \mathbf{r}_1) = e^{-|\mathbf{r}_2 - \mathbf{r}_1|^2/2\delta^2}. \tag{1.3}$$

## 1.2 Creation of a deterministic vortex beam in the source plane

To create a DVB, we take two-dimensional FracFTs with respect to the variables $\mathbf{r}_1$ and $\mathbf{r}_2$. The most elegant approach to do this is to first write the Schell-model degree of coherence of the beam in terms of its Fourier transform,

$$\mu_0(\mathbf{R}) = \int \tilde{\mu}_0(\mathbf{K}) e^{i\mathbf{K}\cdot\mathbf{R}} d^2K, \tag{1.4}$$

where

$$\tilde{\mu}_0(\mathbf{K}) = \frac{1}{(2\pi)^2} \int e^{-R^2/2\delta^2} e^{-i\mathbf{K}\cdot\mathbf{R}} d^2R = \frac{\delta^2}{\pi} e^{-K^2\delta^2/2}. \tag{1.5}$$

The cross-spectral density may then be expressed in the form,

$$W_0(\mathbf{r}_1, \mathbf{r}_2) = \int \tilde{\mu}_0(\mathbf{K}) U_0^*(\mathbf{r}_1, \mathbf{K}) U_0(\mathbf{r}_2, \mathbf{K}) d^2K, \tag{1.6}$$

where $U_0(\mathbf{r}, \mathbf{K})$ represents a monochromatic tilted vortex beam,

$$U_0(\mathbf{r}, \mathbf{K}) = \frac{(x + iy)}{\sigma} e^{-r^2/2\sigma^2} e^{i\mathbf{K}\cdot\mathbf{r}}. \tag{1.7}$$

A FracFT is a generalization of the classical Fourier transform with an order parameter $\alpha$[33]. The transform is defined such that $\alpha = 0$ represents the identity operation and $\alpha = \pi/2$ represents the ordinary Fourier transform operation. The FracFT can be implemented optically using a single lens system, as proposed by Lohmann [34].

The 2-D FracFT can be expressed as an integral transform [35],

$$U_\alpha(\mathbf{r}, \mathbf{K}) = \int_{-\infty}^{\infty} \mathrm{F}_\alpha(\mathbf{r}, \mathbf{r}') U_0(\mathbf{r}', \mathbf{K})\, d^2r', \tag{1.8}$$

where $\mathrm{F}_\alpha(\mathbf{r}, \mathbf{r}')$ represents the 2-D FracFT kernel defined as

$$\mathrm{F}_\alpha(\mathbf{r}, \mathbf{r}') = \frac{ie^{-i\alpha}}{2\pi\sigma^2 \sin\alpha} e^{\frac{-i\cot\alpha r^2}{2\sigma^2}} e^{\frac{i\mathbf{r}\cdot\mathbf{r}'}{\sigma^2 \sin\alpha}} e^{-\frac{i\cot\alpha r'^2}{2\sigma^2}}. \tag{1.9}$$

The FracFT is typically defined as a transform over dimensionless variables; to implement it in transforming a beam, we had to choose a length scale for the transform. In Eq. (1.9), this scale is taken as $\sigma$ so that the beam width of the FracFT tilted beams is independent of the choice of the FracFT order $\alpha$ in the source plane.

After applying the FracFT to the tilted beams in the source plane, Fresnel diffraction can be used to propagate them to any desired distance. The field distribution

along propagation is expressed as

$$U_\alpha(\mathbf{r},\mathbf{K},z) = \int\int \mathrm{G}(\mathbf{r},\mathbf{r}')\mathrm{F}_\alpha(\mathbf{r}',\mathbf{r}'')U_0(\mathbf{r}'',\mathbf{K})d^2r''d^2r', \tag{1.10}$$

Where $\mathrm{G}(\mathbf{r},\mathbf{r}')$ is the Fresnel diffraction kernel, given by

$$\mathbf{G}(\mathbf{r},\mathbf{r}') = \frac{e^{ikz}}{i\lambda z} e^{\frac{ik|\mathbf{r}-\mathbf{r}'|^2}{2z}}. \tag{1.11}$$

Evaluating the integrals of Eq. (1.10), we find the fractional Fourier field propagated to a distance $z$ has the form,

$$\begin{aligned} U_\alpha(\mathbf{r},\mathbf{K},z) =& \frac{-e^{ikz}e^{-i\alpha}}{4\beta^4A^2\sigma} e^{\frac{-(\sin\alpha+i\cos\alpha)}{4\beta^2A\sigma^2}r^2} e^{\frac{-\mathbf{K}\cdot\mathbf{r}}{2\beta^2A}} \\ & e^{\frac{-K^2}{4A}}[(x+K_x\beta^2)+i(y+K_y\beta^2)]. \end{aligned} \tag{1.12}$$

In this expression,

$$\beta^2 \equiv \sigma^2\sin\alpha - \frac{z}{k}\cos\alpha, \tag{1.13}$$

and

$$A \equiv \frac{i\tilde{\beta}^2}{2\beta^2\sigma^2} + \frac{1}{2\sigma^2}, \tag{1.14}$$

$$\tilde{\beta}^2 \equiv \sigma^2\cos\alpha + \frac{z}{k}\sin\alpha. \tag{1.15}$$

It is to be noted that each tilted beam has a vortex at the shifted position $\beta^2\mathbf{K}$; however, if $\beta^2 = 0$, every tilted beam will have its vortex at the origin, and the cross-spectral density will therefore also have a deterministic vortex at the origin. Solving $\beta^2 = 0$ for $z$, we find that we recover the Schell-model vortex beam at distance

$$z_0 = k\sigma^2\tan\alpha. \tag{1.16}$$

Because the tangent function takes on all positive values from zero to infinity as $\alpha$ ranges from 0 to $\pi/2$, we may choose our source parameters to produce a deterministic vortex at any desired propagation distance.

## 1.3 Propagation of a deterministic vortex beam in free space

We may determine the cross-spectral density by a formula analogous to Eq. (1.6),

$$W_\alpha(\mathbf{r}_1, \mathbf{r}_2, z) = \int \tilde{\mu}_0(\mathbf{K}) U_\alpha^*(\mathbf{r}_1, \mathbf{K}, z) U_\alpha(\mathbf{r}_2, \mathbf{K}, z)\, d^2K. \tag{1.17}$$

Substituting from Eq. (1.5) and Eq. (1.12) into the above integral yields

$$\begin{aligned} W_\alpha(\mathbf{r}_1, \mathbf{r}_2, z) = \frac{\delta^2}{16\beta^8 |A|^4 \sigma^2} & e^{-\frac{(\sin\alpha + i\cos\alpha)}{4\beta^2 A \sigma^2} r_2^2} e^{-\frac{(\sin\alpha - i\cos\alpha)}{4\beta^2 A^* \sigma^2} r_1^2} e^{\frac{(\mathbf{r}_1 A + \mathbf{r}_2 A^*)^2}{16\beta^4 |A|^4 \eta}} \\ & \left\{ \frac{1}{\eta^3} \left[ (\eta - \frac{1}{4A})(x_2 + iy_2) - \frac{1}{4A^*}(x_1 + iy_1) \right] * \right. \\ & \left. \left[ (\eta - \frac{1}{4A^*})(x_1 - iy_1) - \frac{1}{4A}(x_2 - iy_2) \right] + \frac{\beta^4}{\eta^2} \right\}, \end{aligned} \tag{1.18}$$

where $\eta \equiv \frac{\delta^2}{2} + \frac{1}{4A} + \frac{1}{4A^*}$. A detailed derivation process of the CSD along propagation is included in the Supplemental Material. The phase of this cross-spectral density will manifest a deterministic vortex at the distance $z_0$.

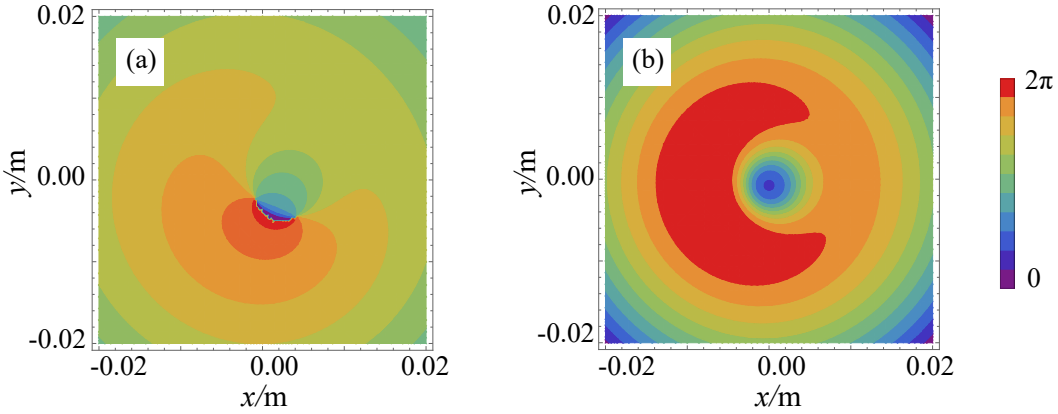


Figure 1.1: Phase of the cross-spectral density of a DVB in the source plane. Here $\alpha = 0.308$, $\sigma = 5 \times 10^{-3}$m, $\delta = 0.01$m. The observation point $\mathbf{r}_1$ is located at (a) (0.3mm,0.3mm), (b) (0.1mm,0mm).

For the following examples, the beam waist width is set to 5 mm and the wave number $k = \frac{2\pi}{5} \times 10^7$ m$^{-1}$. Figure 1.1 shows the phase of the CSD in the source plane $z = 0$ for different values of the observation point $\mathbf{r}_1$. It can be seen that the positions of the vortices, if they even exist, depend upon the position of the observation point, and are therefore singularities of the correlation function and not deterministic vortices. In Fig. 1.1(b), the two correlation vortices have even in fact annihilated, leaving no singularities in the beam.

Figure 1.2 shows the phase of the cross-spectral density and the spectral density in the vicinity of the special distance, here chosen to be $z_0 = 100$ m, with $\alpha = 0.308$. Figures 1.2(a)-(c) show the phase distribution at different propagation distances; the circle indicates the radius $\sigma$ of the beam width for scale. It can be seen that there is a single vortex at the special distance $z_0$, and as one moves away from the special distance the CSD has a pair of opposite-handed vortices in the correlation function. Figure 1.2(d) shows the cross-section of the spectral density along propagation; the green line indicates the position $z_0$.

These deterministic vortices of the DVBs only appear over a finite range around the distance $z_0$. We may estimate this "depth of field" of deterministic vortices as the range over which the single deterministic vortex is the only one that appears within a circle with the radius of the beam width. In Fig. 1.2, it can be seen that from $z = 77$ m to $z = 123$ m there is always only one phase singularity in the beam center within the beam width, making the depth of field approximately 46m for this case. Additional simulations for a variety of choices of $\mathbf{r}_1$ suggest that within this depth of field, the position of the vortex does not depend significantly on the position $\mathbf{r}_1$ of the reference point and that outside this depth of field, the vortex position depends strongly on $\mathbf{r}_1$.

As noted above, these deterministic vortices can be placed at any propagation distance, even quite far away. Figure 1.5 shows the CSD of a DVB for the choice

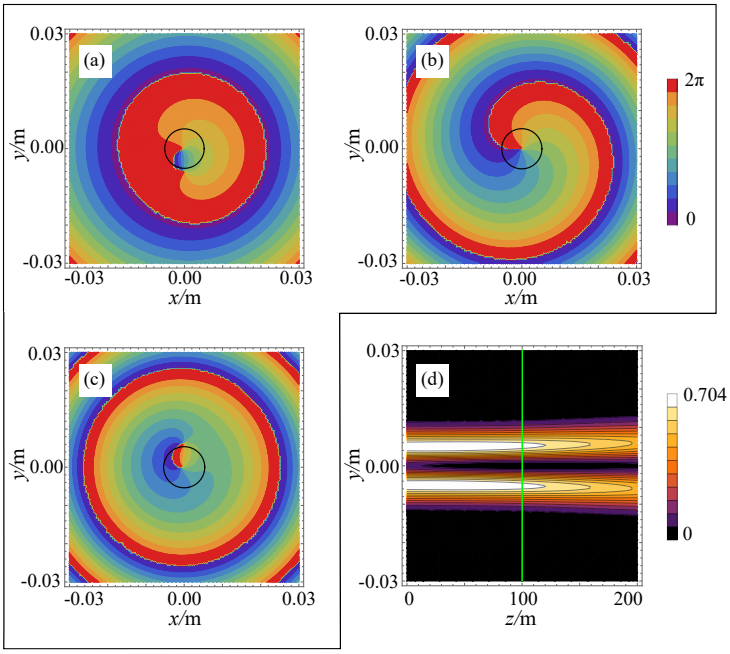


Figure 1.2: Phase of a DVB beam with $z_0 = 100$m. (a) z=77m, (b) z=100m, (c) z=123m; (d) intensity distribution along propagation. Here, in (a)-(c),the observation point $r_1$ is located at (0.1mm,0mm), $\alpha = 0.308$, $\sigma = 5 \times 10^{-3}$m, $\delta = 0.01$m. The black circle represents the radius $\sigma$; in (d) the green line indicates the position where the deterministic vortex is located.

$z_0 = 1000$ m; in this case $\alpha = 1.2664$. The correlation width is still $\delta = 0.01$ m, so that the depth of field is approximately 160m, which within an order of magnitude as the value of Fig. 1.2. This ability to maintain a deterministic vortex in a partially coherent field over long propagation distances has potential application in free-space optical communication and long-range remote sensing.

The correlation width $\delta$ does not affect the position of deterministic vortices, as can be seen by Eq. (1.16). However, it does change the depth of field. Figure 1.4 shows the calculated depth of field over a range of values of the correlation length $\delta$. It can be seen that the depth of field decreases dramatically as the spatial coherence decreases.

Figure 1.5 shows the case $z_0 = 100$ m but $\delta = 0.001$ m. From the selected phase images, it can be seen that the depth of field is reduced to about 0.3 m. Lower spatial

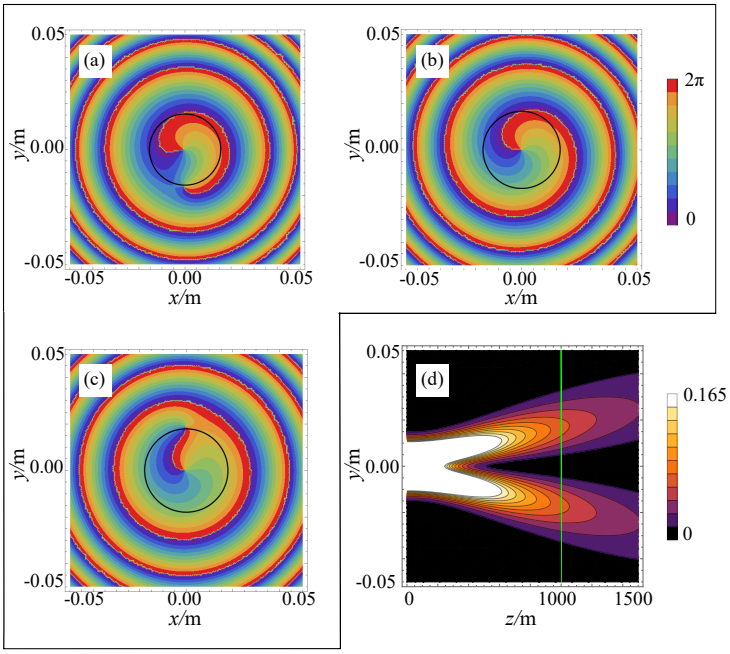


Figure 1.3: Creating a Gaussian Schell-model vortex beam at $z_0 = 1000$m. (a) z=920m, (b) z=1000m, (c) z=1080m; (d) intensity distribution along propagation. Here, $\alpha = 1.2664$, $\sigma = 5 \times 10^{-3}$m, $\delta = 0.01$m.

coherence therefore corresponds with a smaller depth of field. Furthermore, it can be seen from Fig. 1.5(d) that the field exhibits minor self-focusing in this low coherence limit.

This self-focusing effect can be traced to the effect of the FracFT on the constituent components of the beam. Equation (1.12) indicates that, even for $z = 0$, the effect of the FracFT is to tilt the beam in one direction and spatially shift it in the opposite direction. For example, the phase tilt in the $x$-direction is roughly of the form $\exp[iK_x x]$, a positive tilt, while the shift is of the form $(x + K_x\beta^2)$, a negative shift. This naturally creates a converging beam. For beams with low spatial coherence, and contributions from large $\mathbf{K}$ values, this convergence is stronger than the natural diffractive spreading of the beam.

In summary, we have demonstrated that it is possible to design partially coherent beams which manifests a deterministic vortex at any desired propagation distance in free space. In this paper, we only considered a vortex beam of order 1, but deter-

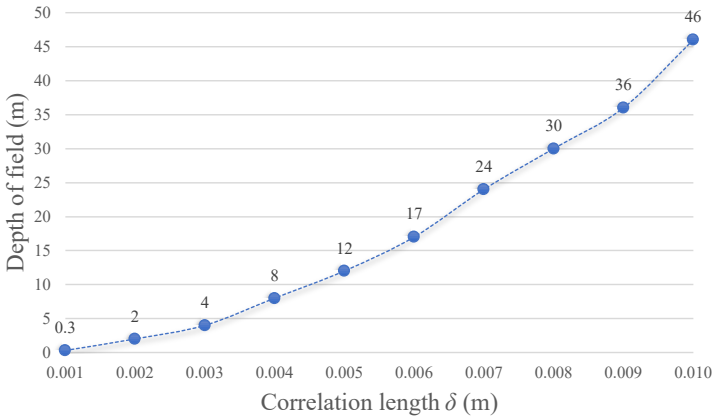


Figure 1.4: Depth of field of the deterministic vortex as correlation length $\delta$ increases from 0.001m to 0.01m. Here, the observation point $r_1$ is located at (0.1mm,0mm), $\alpha = 0.308$, $\sigma = 5 \times 10^{-3}$m.

ministic vortices of any order can in principle be created by changing the order of the GSMV beam at the source. The technique described depends upon the partial undoing of the FracFT transformation by beam propagation, represented by the $\mathbf{r}'$ integration in Eq. (1.10). Furthermore, it is to be noted that the same approach can be applied to any beams with a deterministic vortex, such as Schell-model beams with a higher-order Bessel vortex field profile.

Though FracFTs are often implemented optically using a lens system, it is important to note that such an optical system is not necessary to realize the beams described here. Any method that produces the cross-spectral density of Eq. (1.18) in the source plane will have the same effect. This can be done, for instance, by encoding a spatial light modulator with an appropriate statistical ensemble.

Our results may find use in the synthesis of partial coherence and optical vortices for free-space optical communication. They also demonstrate that the study of the relationship between coherence and singular optics can still yield unexpected effects.

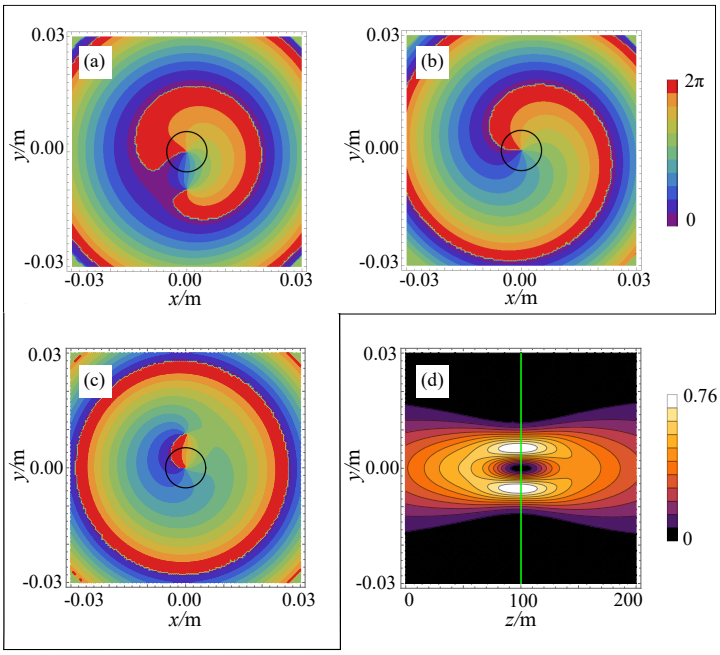


Figure 1.5: Decrease the transverse correlation length $\delta$ to 0.001m. (a) z=99.8m, (b) z=100m, (c) z=100.1m; (d) intensity distribution along propagation. Here, $\alpha = 0.308, \sigma = 5 \times 10^{-3}$m.

# CHAPTER 2: DESIGN OF LISSAJOUS BEAMS

## 2.1 Introduction

Singularities in optical wavefields, such as optical vortices in scalar fields and polarization singularities in vector fields, have become an area of great theoretical and practical interest, becoming the field known as singular optics [36]. Typical optical vortices in a three-dimensional field are lines of zero intensity around which the phase has a circulating or helical structure, and typical polarization singularities in a three-dimensional field are lines on which the state of polarization is circular, with the major axis of the polarization ellipse undefined. Such singularities have been used for diverse applications such as imaging, trapping and rotation of particles, and free-space communications [11].

Most studies of singular optics have focused on fields which are monochromatic or quasi-monochromatic. In 2003, however, Kessler and Freund noted that a new class of singularities could be defined for fields which possess two harmonic frequencies [12], with a fundamental frequency $\omega$ and a first harmonic $2\omega$. The singularities in this case are lines in three-dimensional space where a generalized orientation of the polarization figure, now a Lissajous figure, is undefined. Freund elaborated on the properties of these Lissajous singularities in detail, focusing on the case where the fields are produced by second harmonic generation (SHG) [37].

In recent years, Lissajous singularities have been observed and investigated in a number of projects. These include a study of the dynamical evolution of Lissajous singularities in free-space propagation [38], control of the polarization of Lissajous fields in high-harmonic generation [39], and the topological features of Lissajous fields [40].

Though researchers have suggested a number of potential applications for such polarized bichromatic beams, there has been relatively little work investigating the

properties of beams possessing Lissajous singularities. For example, though fundamental classes of beams containing a single optical vortex or polarization singularity on the propagation axis have been derived, no comparable class of Lissajous beams has been introduced. The second harmonic generation example of Kessler and Freund's original paper [12], for example, contains 4 total Lissajous singularities, three surrounding a central fourth. In this paper, we introduce a class of Lissajous beams, discuss the various types of beams that are possible, and investigate their basic propagation properties.

We consider a bichromatic optical field in the form

$$\mathbf{E}(\mathbf{r}) = \mathbf{A}(\mathbf{r})e^{-i\omega_1 t} + \mathbf{B}(\mathbf{r})e^{-i\omega_2 t}, \tag{2.1}$$

where $\omega_1$ and $\omega_2$ are signal frequencies with the relation of $\omega_2 = 2\omega_1$.

A Lissajous singularity is a polarization singularity in a bichromatic field where the total complex Stokes field equals zero, i.e.

$$S_{12} = S_1 + iS_2 = 0. \tag{2.2}$$

In analogy with the monochromatic case, we define the orientation angle $\phi$ of the bichromatic field as

$$\tan(2\phi) = \frac{S_2}{S_1}, \tag{2.3}$$

where $S_1$ and $S_2$ are the first and second Stokes parameters of the bichromatic field. They are expressed as [41]

$$S_{1,A} = \langle |A_x|^2 - |A_y|^2 \rangle, \quad S_{1,B} = \langle |B_x|^2 - |B_y|^2 \rangle, \tag{2.4}$$

$$S_{2,A} = \langle A_y{}^* A_x + A_x{}^* A_y \rangle, \quad S_{2,B} = \langle B_y{}^* B_x + B_x{}^* B_y \rangle, \tag{2.5}$$

where $S_{1,A}$ and $S_{2,A}$ are the first and second Stokes parameters for $\mathbf{A}(\mathbf{r})$, and $A_x$ and

$A_y$ are the orthogonal field components of $\mathbf{A}(\mathbf{r})$, with similar definitions for $\mathbf{B}(\mathbf{r})$. Because Stokes parameters are additive, the total Stokes parameters in Eq. (1.2) are

$$S_1 = S_{1,A} + S_{1,B}, \quad S_2 = S_{2,A} + S_{2,B}. \tag{2.6}$$

From Eq. (2.6), it is straightforward to see that Lissajous singularities can exist at a point even when there are no singularities in the individual frequency components, as was noted by Freund [42]. All that is necessary is that the states of polarization of the two frequency components lie on opposite sides of the Poincaré sphere. Thus, the most well-known Lissajous singularity with a trefoil pattern is a special case where both frequency components have circular polarization with opposite handedness at a point, and individually have $S_{12} = 0$. There are many more possibilities, however, as we now discuss.

## 2.2 Local forms of an isolated Lissajous singularity

Inspired by the preceding observations, we introduce a local form of an isolated Lissajous singularity where, near the $z$-axis, $\mathbf{A}$ and $\mathbf{B}$ are of the forms,

$$\mathbf{A}(\mathbf{r}) = \gamma_1 \hat{\mathbf{e}}_1 (x + i\beta_1 y)^{m_1} + \hat{\mathbf{e}}_2, \tag{2.7}$$

$$\mathbf{B}(\mathbf{r}) = \gamma_2 \hat{\mathbf{e}}_2 (x + i\beta_2 y)^{m_2} + \hat{\mathbf{e}}_1. \tag{2.8}$$

where

$$\hat{\mathbf{e}}_1 = a_x \hat{\mathbf{x}} + a_y e^{i\delta_A} \hat{\mathbf{y}}, \tag{2.9}$$

$$\hat{\mathbf{e}}_2 = b_x \hat{\mathbf{x}} + b_y e^{i\delta_B} \hat{\mathbf{y}}, \tag{2.10}$$

are unit vectors, which will typically – but not always – taken to be orthogonal. The choice of $\hat{\mathbf{e}}_1$ and $\hat{\mathbf{e}}_2$ directly affect the orientation and handedness of the Lissajous singularity at the origin. The two fields $\mathbf{A}$ and $\mathbf{B}$ are each made of a local vortex

component of order $m_{1,2}$ and a plane wave component; $\gamma_{1,2}$ is generally complex and introduces a relative amplitude and phase difference between the components. The quantity $\beta_{1,2} = \pm 1$ is the handedness of the vortex, and $m_1$ and $m_2$ are non-negative integer orders of the vortex for each frequency.

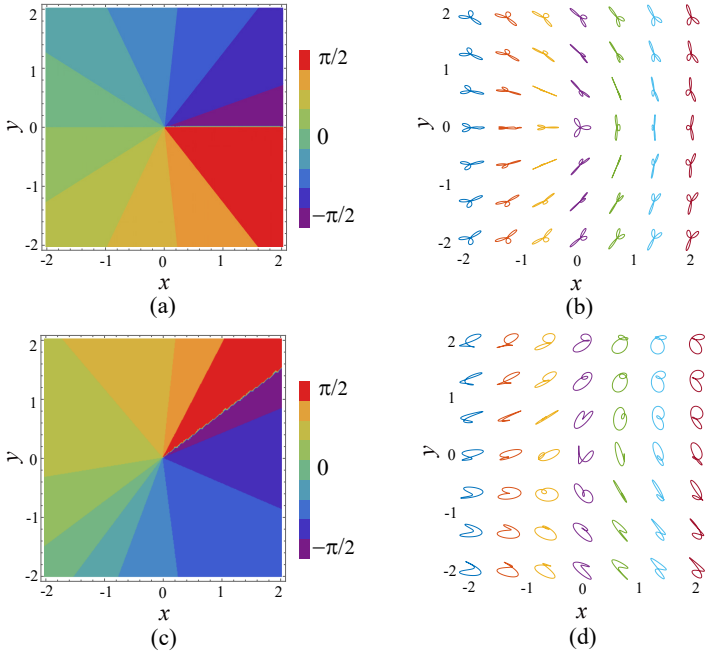


Figure 2.1: Illustration of the polarization state of two fundamental Lissajous patterns.(a)-(b) Lissajous singularity with $m_{1,2} = 1$, $\gamma_{1,2} = 1$, $\beta_1 = -1$, $\beta_2 = 1$, $a_x = \frac{\sqrt{2}}{2}$, $a_y = \frac{\sqrt{2}}{2}$, $b_x = -\frac{\sqrt{2}}{2}$, $b_y = \frac{\sqrt{2}}{2}$, $\delta_A = \delta_B = \pi/2$. (c)-(d) Lissajous singularity with $m_{1,2} = 1$, $\gamma_{1,2} = 1$, $\beta_1 = 1$, $\beta_2 = -1$, $a_x = \frac{\sqrt{2}}{4}$, $a_y = \frac{\sqrt{14}}{4}$, $b_x = -\frac{\sqrt{14}}{4}$, $b_y = \frac{\sqrt{2}}{4}$, $\delta_A = \delta_B = \pi/4$. The colors of (a) and (c) indicate the orientation angle defined by Eq. (1.2), while (b) and (d) show the Lissajous patterns.

Fig. 2.1 shows two examples of Lissajous singularities generated using the above local expressions. The color plots show the orientation angle as a function of position; points where all colors come together represent a singularity of orientation angle, as defined by Eq. (2.3). It can be seen that (a), (b) represent an isolated trefoil singularity, while (c), (d) represent an isolated Lissajous singularity of more general form.

Equations (2.7) and (2.8) have a bewildering number of parameters that can be

adjusted; however, not all of these parameters will result in a single Lissajous singularity in the beam center. Investigations have shown that there are two broad cases where a single singularity exists. The first case, which we will call Type A, is when $\beta_1\beta_2 = -1$ and $m_1 = m_2$, i.e. the vortex components of the fields are of equal and opposite charge. Most arbitrary combinations of $\gamma_1$ and $\gamma_2$ work (but not all the time, for example, $\gamma_1\gamma_2 = -1$ does not produce a single singularity). Curiously, it was found that $\hat{\mathbf{e}}_1$ and $\hat{\mathbf{e}}_2$ can be almost any orthogonal states except for linear states. For linear polarization, the singularity breaks down into a line where $S_{12} = 0$ in the plane.

The second case, which we will call Type B, is when $\gamma_1 = 0$ or $\gamma_2 = 0$. Then $\beta_2$ or $\beta_1$ can be $\pm 1$ and $m_2$ or $m_1$ can be any positive integer. For this case, $\hat{\mathbf{e}}_1$ and $\hat{\mathbf{e}}_2$ are only allowed to be orthogonal circular states. For other bases there will be multiple singularities in the beam cross-section; we will see an example momentarily.

## 2.3 Construct Lissajous beams

We next construct Lissajous beams by replicating the local forms of Eqs. (2.7) and (2.8) with combinations of Laguerre-Gauss beams. The propagation formula for a LG beam with radial index $n = 0$ and waist width $W_{1,2}$ is of the form,

$$\begin{aligned}\mathbf{E}^{LG}_{m_{1,2}}(\rho,\phi,z) =& \frac{1}{\sqrt{[|m_{1,2}|]!}}\left[\frac{\sqrt{2}\rho}{w_{1,2}(z)}\right]^{|m_{1,2}|} \\ & \times e^{i\beta_{1,2}m_{1,2}\phi}\mathbf{E}^{G}_{1,2}(\mathbf{r})e^{-i(|m_{1,2}|)\Phi_{1,2}(z)}\end{aligned} \tag{2.11}$$

where $\mathbf{E}^{LG}_{m_i}$ represents the vortex component of the field with frequency $\omega_i$, and

$$\mathbf{E}^{G}_{1,2}(\rho,\phi,z) = A_0 e^{-i\Phi_{1,2}(z)}\frac{e^{\frac{ik_{1,2}\rho^2}{2R_{1,2}(z)}}}{\sqrt{1+z^2/z^2_{1,2}}}e^{\frac{-\rho^2}{w^2_{1,2}(z)}} \tag{2.12}$$

represents a fundamental Gaussian beam with $A_0 = 1$ . The quantity $R_{1,2}(z)$ represents the wavefront curvature, $w_{1,2}(z)$ is the propagation-dependent beam width, $\Phi_{1,2}(z)$ is the Gouy phase and $z_{1,2}$ the Rayleigh range, $z_{1,2} = W_{1,2}^2 k_{1,2}/2$.

We write our proposed Lissajous beams in the form,

$$\mathbf{E}(\rho, \phi, z) = \mathbf{E_1}(\rho, \phi, z)e^{-i\omega_1 t} + \mathbf{E_2}(\rho, \phi, z)e^{-i\omega_2 t} \tag{2.13}$$

where

$$\mathbf{E_1}(\rho, \phi, z) = \gamma_1 \hat{\mathbf{e}}_\mathbf{1} \mathbf{E}_{m_1}^{LG}(\rho, \phi, z) + \hat{\mathbf{e}}_\mathbf{2} \mathbf{E}_1^G(\rho, \phi, z), \tag{2.14}$$

$$\mathbf{E_2}(\rho, \phi, z) = \gamma_2 \hat{\mathbf{e}}_\mathbf{2} \mathbf{E}_{m_2}^{LG}(\rho, \phi, z) + \hat{\mathbf{e}}_\mathbf{1} \mathbf{E}_2^G(\rho, \phi, z). \tag{2.15}$$

We begin our simulations by investigating Lissajous beams in the source plane $z = 0$ and we take $W_{1,2} = 10^{-2} m$ for both frequency components. It is to be noted that all of the following plots have sizes which are comparable to the intensity spot; the figures therefore show the full range of Lissajous patterns covered in the beam cross-section. Furthermore, in the source plane the Lissajous figures are independent of the choice of carrier and signal frequencies.

If a beam possesses only one Lissajous singularity in the beam profile that lies in the center, we refer to it as a pure Lissajous beam; other cases that can be derived from Eqs. (2.7) and (2.8) we refer to as non-pure Lissajous beams. We now look at a variety of examples.

Fig. 3.2 shows two examples of pure Type A Lissajous beams. We can see that by choosing $\beta_1 = -1$ and $\beta_2 = 1$, the orientation of polarization changes from $\pi/2$ to $-\pi/2$ following a clockwise path for both $m_1 = m_2 = 1$ and $m_1 = m_2 = 3$. If we choose $\beta_1 = 1$ and $\beta_2 = -1$, the orientation will change in the opposite direction.

Fig. 2.3 shows two examples of pure Type B Lissajous beams, for which $\gamma = 0$ for one of the frequency field components and $\hat{\mathbf{e}}_\mathbf{1}$ and $\hat{\mathbf{e}}_\mathbf{2}$ can only be orthogonal circular

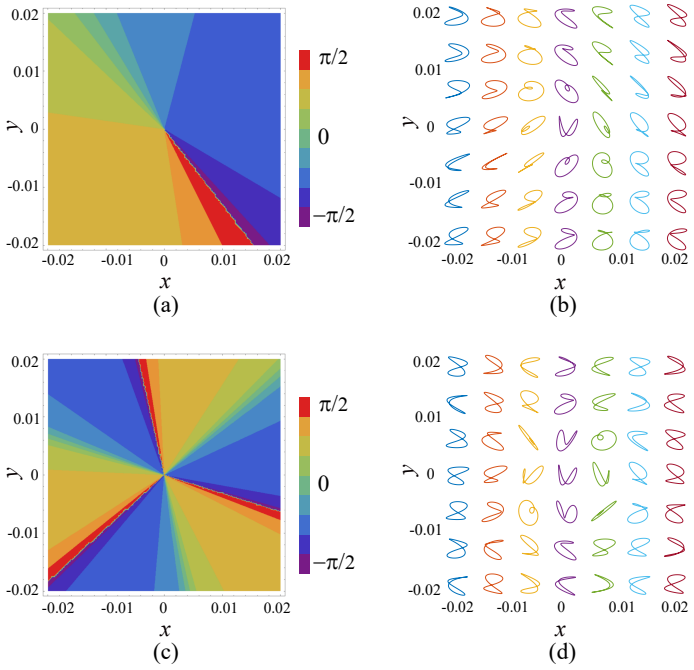


Figure 2.2: Examples of pure Type A Lissajous beams, with (a)-(b) $m_{1,2} = 1$,(c)-(d) $m_{1,2} = 3$. In both cases, we take $\gamma_{1,2} = 1, \beta_1 = -1, \beta_2 = 1, a_x = \frac{1}{6}, a_y = \frac{\sqrt{35}}{6}, b_x = -\frac{\sqrt{35}}{6}, b_y = \frac{1}{6}, \delta_A = \delta_B = \pi/5$.

polarization states. Though the vortex order is different for both examples, we get the same trefoil pattern at the center of each beam; this pattern depends only on the choice of polarization basis.

It is worthwhile to explore the behavior of non-pure beams as well. In Fig. 3.4(a)-(b), we investigate a beam with the same parameters as in Fig. 3.2, except we replace $\beta_1\beta_2 = -1$ with $\beta_1\beta_2 = 1$, i.e. the vortex charges are equal rather than opposite. It can be seen that there are no point Lissajous singularities, but instead there are spoke-like Lissajous singularity lines, along which the orientation jumps by $\pi/2$. Alternatively, we may keep all the parameters the same as in Fig. 2.3, except we now allow $\hat{\mathbf{e}}_1$ and $\hat{\mathbf{e}}_2$ to be orthogonal elliptical states, in general resulting in more than one singularity in the beam profile. In Fig. 2.4(c)-(d), now there is one third-order positive singularity on axis and three negative singularities off axis.

Returning again to pure beams, we now investigate how these beams evolve on

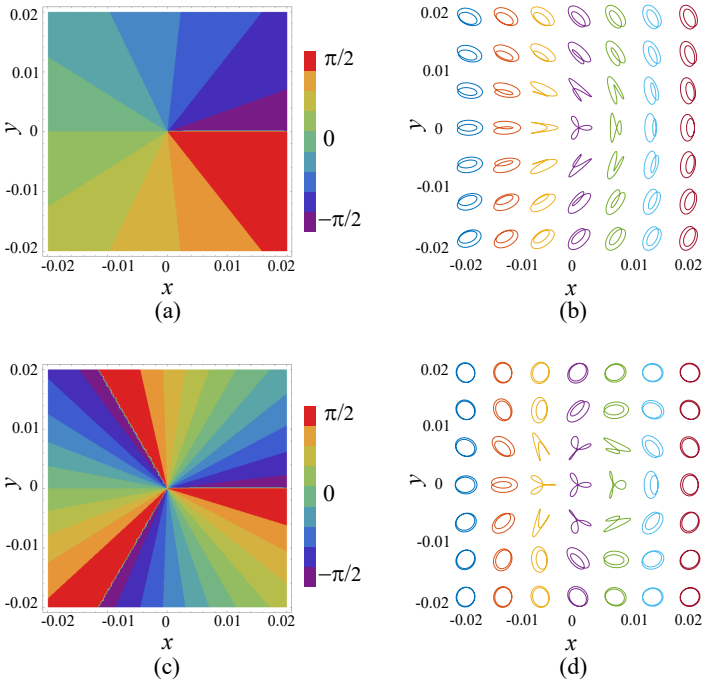


Figure 2.3: Examples of pure Type B Lissajous beams, with (a)-(b) $m_2 = 1$,(c)-(d) $m_2 = 3$. In both cases, we take $\gamma_1 = 0, \gamma_2 = 1, \beta_2 = 1, a_x = \frac{\sqrt{2}}{2}, a_y = \frac{\sqrt{2}}{2}, b_x = -\frac{\sqrt{2}}{2}, b_y = \frac{\sqrt{2}}{2}, \delta_A = \delta_B = \pi/2$.

propagation. We consider a SHG example, with $k_1 = \frac{2\pi}{5} \times 10^7$, $k_2 = \frac{4\pi}{5} \times 10^7$. We estimate the Rayleigh range for the bichromatic field as an approximate average of the Rayleigh ranges $z_1$ and $z_2$ of the two frequency components; for our choice of beam widths and frequencies, this width is 1 km. The polarization distribution is examined both in the near field ($z = 1$ m) and at the Rayleigh range for a pure Type A beam in Fig. 2.5.

It can be seen that the center singularity remains even after propagating to the Rayleigh range, and that no new singularities appear; we find similar results for other higher-order pure Lissajous beams. The trefoil pattern remains a trefoil but its orientation changes and its curvature changes. This is shown in more detail in Fig. 2.6(a)-(c). Even more dramatic changes in the shape will arise if the two frequency components of the beam have different spatial widths, which results in different propagation characteristics, as seen in Fig. 2.6(d)-(f).

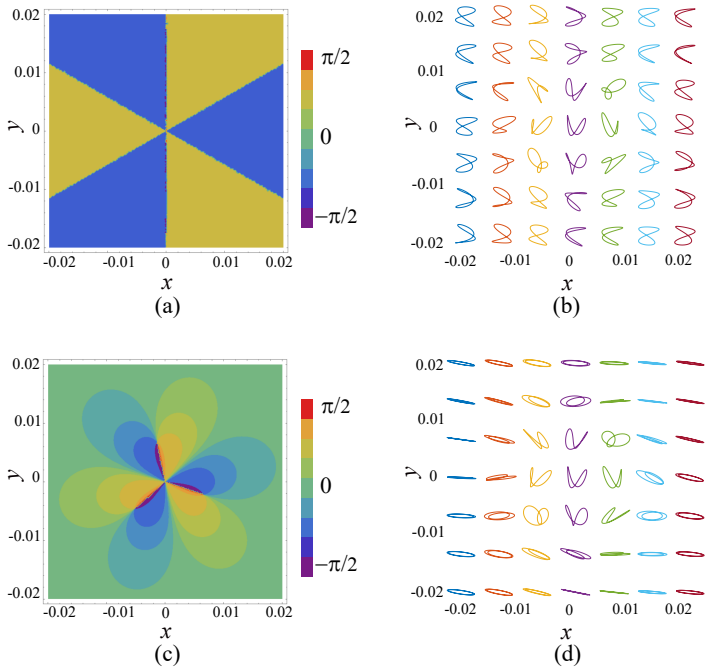


Figure 2.4: Non-pure Lissajous beams, with (a)-(b) $m_{1,2} = 3, \gamma_{1,2} = 1, \beta_{1,2} = 1$; (c)-(d) $m_2 = 3, \gamma_1 = 0, \gamma_2 = 1, \beta_2 = 1$. For both cases, $a_x = \frac{1}{6}, a_y = \frac{\sqrt{35}}{6}, b_x = -\frac{\sqrt{35}}{6}, b_y = \frac{1}{6}, \delta_A = \delta_B = \pi/5$.

The changes in shape can be roughly understood by calculating the field on axis of the two components from Eqs. (2.11) and (2.12),

$$\mathbf{E_1}(0, \phi, z) = A_0 \frac{e^{-i\Phi_1(z)}}{\sqrt{1 + z^2/z_1^2}} \hat{\mathbf{e}}_\mathbf{2}, \tag{2.16}$$

$$\mathbf{E_2}(0, \phi, z) = A_0 \frac{e^{-i\Phi_2(z)}}{\sqrt{1 + z^2/z_2^2}} \hat{\mathbf{e}}_\mathbf{1}. \tag{2.17}$$

Eqs. (2.16) and (2.17) show that the amplitudes of the two components and their Gouy phases are $z$-dependent, depending on the relative beam waists and frequencies. A relative shift in amplitude will change the shape of the Lissajous figure, while the relative change in phase will affect the amplitude of the figure. Because the Gouy phase shift for a Gaussian always changes by $\pi/2$ at most, we expect that the maximum change in orientation is also $\pi/4$, which follows from Eq. (3.7).

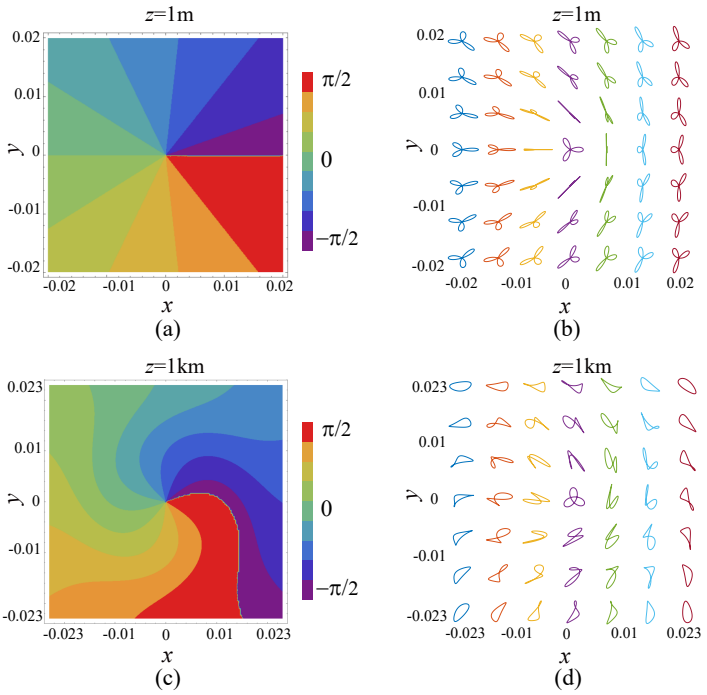


Figure 2.5: Propagation of a pure Lissajous beam. $m_{1,2} = 1, \gamma_{1,2} = 1, \beta_1 = -1, \beta_2 = 1, a_x = \frac{\sqrt{2}}{2}, a_y = \frac{\sqrt{2}}{2}, b_x = -\frac{\sqrt{2}}{2}, b_y = \frac{\sqrt{2}}{2}, \delta_A = \delta_B = \pi/2$.

It is to be noted that, for very long propagation distances, the components of the beam can change enough to cause new singularities to manifest. However, for all examples we have considered, this only happens after the Rayleigh distance, which means the beams will have a propagation-invariant singularity that travels for at least 1 km for the parameter choices given here.

In summary, we have demonstrated that it is possible to create a class of pure Lissajous beams which possess a solitary on-axis Lissajous singularity, and that these beams can maintain this structure over significant propagation distances. These results lay a foundation for the application of bichromatic optical singularities.

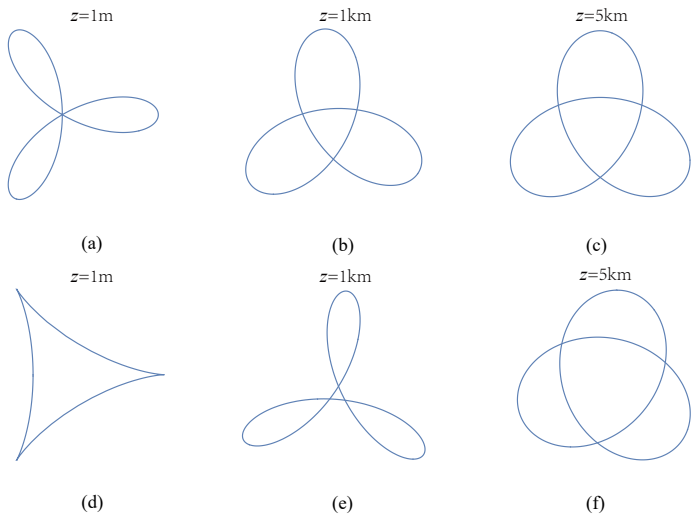


Figure 2.6: Evolution of on-axis Lissajous singularity along propagation. (a)-(c) $W_1 = W_2 = 10^{-2}m$, (d)-(f) $W_1 = 10^{-2}m, W_2 = 2 * 10^{-2}m$.

# CHAPTER 3: LISSAJOUS SINGULARITIES IN YOUNG'S INTERFERENCE EXPERIMENT

Singularities in wavefields have become important objects of study, both for their unusual physical properties and the use of those properties to improve optical systems. The classic singularities are optical vortices in scalar wavefields, which are lines of zero intensity in three-dimensional space around which the phase has a circulating or helical structure [2, 43]. Beams with optical vortices have been used for a variety of applications, including free-space optical communications [21], super-resolved imaging [44], and coronagraphy [45].

In vector electromagnetic fields, optical vortices are not typically seen and instead the typical singularities encountered are polarization singularities [46], which for paraxial fields include lines of circular polarization (on which the orientation of the polarization ellipse is undefined) and surfaces of linear polarization (on which the handedness of the polarization ellipse is undefined). Polarization singularities have also been used for a number of applications, including imaging [47, 48] and light-matter manipulation [49].

Both optical vortices and polarization singularities are typically studied in monochromatic fields. It is possible to generalize them further, however, and consider the types of singularities that appear in bichromatic fields where the higher frequency is a harmonic of the lower. The electric field vector then traces out a Lissajous figure instead of an ellipse; singularities of the generalized orientation of this figure are called Lissajous singularities, and were first introduced by Freund and Kessler [12, 50]. These singularities, like polarization singularities and optical vortices, have potential to be used in imaging and communications, and recently a class of beams containing a single Lissajous singularity at their core was formulated [51].

Though the topology of Lissajous singularities has been well-formulated, the conditions under which Lissajous singularities can be formed, for example through inter-

ference, are still unclear. Young's interference experiment provides a unique platform for exploring a rich variety of phenomena in both classical optics and quantum optics [13]. In 2003, it was used to investigate singularities of the correlation function that appear in partially coherent light [52]. In 2009, the experiment was used to analyze the creation of polarization singularities [53]. It is natural, then, to consider Young's experiment for bichromatic fields in order to determine conditions under which Lissajous singularities can be created in interference.

In this study, we use Young's interference experiment to investigate the superposition of two vector beams, each possessing two frequency components, and we derive sufficiency conditions under which the Lissajous-type polarization singularities are formed on the observation screen. We give examples of the Lissajous patterns and singularities created under these conditions, and demonstrate additional cases of singularity creation.

## 3.1 Introduction to Lissajous singularities

Consider a beam-like electromagnetic field traveling along the $z$-direction, and containing frequencies $\omega_a$ and $\omega_b$. At position $\mathbf{r}$ and time $t$, its electric field can be expressed as

$$\mathbf{E}(\mathbf{r}) = \mathrm{Re}\left[\mathbf{A}(\mathbf{r})e^{-\mathrm{i}\omega_a t} + \mathbf{B}(\mathbf{r})e^{-\mathrm{i}\omega_b t}\right], \tag{3.1}$$

where $\mathbf{A}$ and $\mathbf{B}$ are complex vectors with $x$ and $y$-components. Because these vectors are complex, a complete characterization of the electric field requires eight real numbers. In a circular polarization basis with unit vectors

$$\boldsymbol{\epsilon}_{\pm} = \frac{1}{\sqrt{2}}(\hat{\mathbf{x}} \pm \mathrm{i}\hat{\mathbf{y}}), \tag{3.2}$$

the electric field at each point and at each individual frequency can be written as

$$\mathbf{E} = E_l \boldsymbol{\epsilon}_+ + E_r \boldsymbol{\epsilon}_-, \tag{3.3}$$

with $E_l$ and $E_r$ the complex amplitude of the left- and right-handed component, respectively. The four Stokes parameters may be written as [54]

$$S_0 = |E_l|^2 + |E_r|^2, \tag{3.4}$$

$$S_1 = 2\ \mathrm{Re}[E_l^* E_r], \tag{3.5}$$

$$S_2 = 2\ \mathrm{Im}[E_l^* E_r], \tag{3.6}$$

$$S_3 = |E_l|^2 - |E_r|^2. \tag{3.7}$$

Using the circular basis allows us to take advantage of the simple relation between $S_1$ and $S_2$, as we will see. Because the Stokes parameters are cycle-averaged, those of the total bichromatic field are simply the sum of the parameters at each of the two frequencies, i.e.,

$$S_j = S_{j,a} + S_{j,b}, \quad j \in \{0, 1, 2, 3\}. \tag{3.8}$$

In analogy with polarization singularities in a monochromatic field, two types of singularities can occur in a bichromatic field [50]: singularities of handedness and singularities of orientation. Because the latter is a direct analogue of vortices, it has broad potential applications compared to singularities of handedness which are surfaces in 3-D. Thus, this paper focuses exclusively on Lissajous singularities of orientation, hereafter referred to as Lissajous singularities.

A Lissajous singularity is a polarization singularity in a bichromatic field where the total complex Stokes field $S_{12}$ equals zero, i.e.

$$S_{12} \equiv S_1 + \mathrm{i}S_2 = 0, \tag{3.9}$$

which means a Lissajous singularity only appears when $S_1$ and $S_2$ both equal 0. At a singularity, the pattern's orientation angle with respect to the $x$-axis is undefined; this orientation angle is given by [12]

$$\tan(2\psi) = \frac{S_2}{S_1}. \tag{3.10}$$

In a bichromatic field, a singularity of orientation is not a simple figure like circular polarization in the monochromatic case, but is generally a Lissajous figure.

## 3.2 Bichromatic version of Young's experiment

Let us consider Young's setup, as sketched in Fig. 3.1, in which a bichromatic beam, with frequencies $\omega_a$ and $\omega_b$ and corresponding wavenumbers $k_a$ and $k_b$, is normally incident on a screen $\mathcal{A}$ that contains two identical pinholes separated by a distance $d$. The polarization state at the two frequencies need not be equal, and may be different at each pinhole. The superposition of the fields emanating from the apertures $Q_1$ and $Q_2$ is observed at a point $P = (x, 0, \Delta z)$ on a second, parallel screen $\mathcal{B}$.

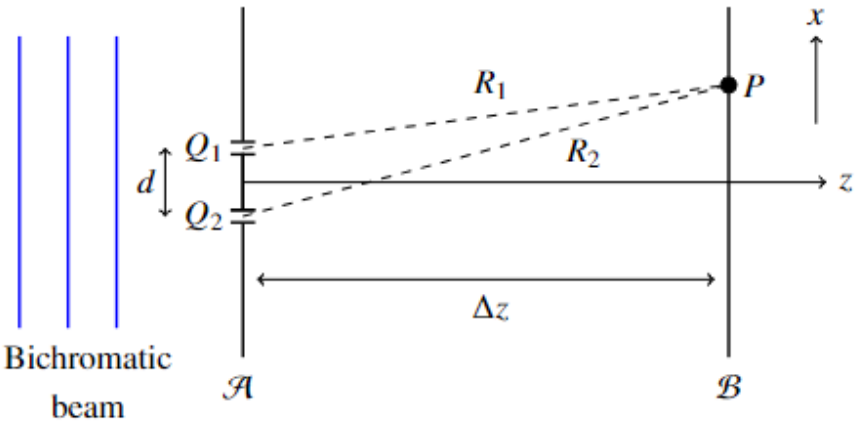


Figure 3.1: Young's experiment with two frequencies. A bichromatic beam is incident on screen $\mathcal{A}$ in the plane $z = 0$, which contains two identical pinholes, $Q_1$ at $(d/2, 0, 0)$, and $Q_2$ at $(-d/2, 0, 0)$. The observation screen $\mathcal{B}$ is located in the plane $z = \Delta z$. The two distances (dashed lines) are $R_1 = Q_1P$ and $R_2 = Q_2P$.

At frequency $\beta$ (with $\beta = a, b$), the transverse field at $P$ has the form

$$\mathbf{E}_\beta(P) = A_{1,\beta}K_{1,\beta}\hat{\mathbf{e}}_{1,\beta}e^{\mathrm{i}k_\beta R_1} + A_{2,\beta}K_{2,\beta}\hat{\mathbf{e}}_{2,\beta}e^{\mathrm{i}k_\beta R_2}. \tag{3.11}$$

Here, $A_{i,\beta}$ represents the amplitude of the field at the $\beta$th frequency emanating from the aperture $Q_i$, and $\hat{\mathbf{e}}_{i,\beta}$, with $i = 1, 2$, is a unit polarization vector expressed in the circular basis, as indicated in Eq. (3.2), that characterizes the polarization state at the aperture $Q_i$. Explicitly,

$$\hat{\mathbf{e}}_{i,\beta} = p_{i,\beta}\boldsymbol{\epsilon}_+ + m_{i,\beta}\boldsymbol{\epsilon}_-, \tag{3.12}$$

with $|p_{i,\beta}|^2 + |m_{i,\beta}|^2 = 1$. We shall take $p_{i,\beta}$ to be complex while $m_{i,\beta}$ is assumed to be real. The propagator $K_{i,\beta}$ is given by the expression [55]

$$K_{i,\beta} = \frac{d\mathcal{A}}{\mathrm{i}\lambda_\beta R_i}, \tag{3.13}$$

where $d\mathcal{A}$ is the pinhole area, and $\lambda_\beta = 2\pi/k_\beta$. Under typical circumstances the two distances $x$ and $d$ are much smaller than the screen separation $\Delta z$. We then have to a good approximation

$$R_2 - R_1 \approx \frac{xd}{\Delta z}, \tag{3.14}$$

and

$$K_{1,\beta} \approx K_{2,\beta} = K_\beta. \tag{3.15}$$

In our derivation we make use of these two approximations, but in the simulations the exact form of the expressions will be used.

Because the propagator depends on $\lambda_\beta$, as seen in Eq. (3.13) the apertures will preferentially transmit more light of the smaller wavelength component. This will cause the smaller wavelength to dominate on the observation screen and wash out any

Lissajous singularities. To eliminate the difference in amplitude at the two frequencies caused by their respective propagators, we let $A_{i,\beta} = 1/K_\beta$, to obtain a normalized vector field

$$\bar{\mathbf{E}}_\beta(P) = \hat{\mathbf{e}}_{1,\beta} e^{\mathrm{i}k_\beta R_1} + \hat{\mathbf{e}}_{2,\beta} e^{\mathrm{i}k_\beta R_2}. \tag{3.16}$$

This could be done experimentally by placing appropriate spectral filters in front of the pinholes $Q_i$.

The resulting normalized Stokes parameters at frequency $\beta$ on the observation screen are thus

$$\bar{S}_{1,\beta}(P) = 2\ \mathrm{Re}[\bar{E}^*_{l,\beta}(P)\bar{E}_{r,\beta}(P)], \tag{3.17}$$

$$\bar{S}_{2,\beta}(P) = 2\ \mathrm{Im}[\bar{E}^*_{l,\beta}(P)\bar{E}_{r,\beta}(P)], \tag{3.18}$$

where

$$\bar{E}_{l,\beta}(P) = \bar{E}_\beta(P) \cdot \boldsymbol{\epsilon}^*_+, \tag{3.19}$$

$$\bar{E}_{r,\beta}(P) = \bar{E}_\beta(P) \cdot \boldsymbol{\epsilon}^*_-. \tag{3.20}$$

For brevity we omit, from now on, the dependence on the position $P$. At frequency $a$ we thus have

$$\bar{S}_{1,a} = 2\ \mathrm{Re}\left[\left(p^*_{1,a} e^{-\mathrm{i}k_a R_1} + p^*_{2,a} e^{-\mathrm{i}k_a R_2}\right)\left(m_{1,a} e^{\mathrm{i}k_a R_1} + m_{2,a} e^{\mathrm{i}k_a R_2}\right)\right], \tag{3.21}$$

$$\bar{S}_{2,a} = 2\ \mathrm{Im}\left[\left(p^*_{1,a} e^{-\mathrm{i}k_a R_1} + p^*_{2,a} e^{-\mathrm{i}k_a R_2}\right)\left(m_{1,a} e^{\mathrm{i}k_a R_1} + m_{2,a} e^{\mathrm{i}k_a R_2}\right)\right]. \tag{3.22}$$

Similar expressions are obtained for $\bar{S}_{1,b}$ and $\bar{S}_{2,b}$. Using their additive property, the

Stokes parameters for the total field on the observation screen are thus

$$\bar{S}_1 = \bar{S}_{1,a} + \bar{S}_{1,b}, \tag{3.23}$$

$$\bar{S}_2 = \bar{S}_{2,a} + \bar{S}_{2,b}. \tag{3.24}$$

It is to be noted that the there are two ways to get a Lissajous singularity at a point: the Stokes vectors can be identically zero at each frequency, or the different frequency components can cancel each other out.

## 3.3 Lissajous singularities in Young's experiment

Lissajous singularities appear at points where the zeros of $\bar{S}_1$ and $\bar{S}_2$ coincide. Since these two parameters are the real and imaginary part of the same expression, it readily follows that these joint zeros imply a single condition, i.e.,

$$\begin{aligned} &p_{1,a}^* \left[m_{1,a} + m_{2,a} e^{\mathrm{i}k_a(R_2-R_1)}\right] + p_{2,a}^* \left[m_{2,a} + m_{1,a} e^{-\mathrm{i}k_a(R_2-R_1)}\right] \\ &+ p_{1,b}^* \left[m_{1,b} + m_{2,b} e^{\mathrm{i}k_b(R_2-R_1)}\right] + p_{2,b}^* \left[m_{2,b} + m_{1,b} e^{-\mathrm{i}k_b(R_2-R_1)}\right] = 0. \end{aligned} \tag{3.25}$$

Eq. (3.25) can be rewritten in a compact matrix form as

$$\langle \mathbf{A}|\mathbf{M}|\mathbf{A}\rangle^\dagger = 0. \tag{3.26}$$

Here

$$\langle \mathbf{A}| = \begin{bmatrix} e^{-\mathrm{i}k_a R_1} & e^{-\mathrm{i}k_a R_2} & e^{-\mathrm{i}k_b R_1} & e^{-\mathrm{i}k_b R_2} \end{bmatrix}, \tag{3.27}$$

$|\mathbf{A}\rangle^\dagger$ is the adjoint of $\langle \mathbf{A}|$, and

$$\mathbf{M} = \begin{bmatrix} p_{1,a}^* m_{1,a} & p_{1,a}^* m_{2,a} & 0 & 0 \\ p_{2,a}^* m_{1,a} & p_{2,a}^* m_{2,a} & 0 & 0 \\ 0 & 0 & p_{1,b}^* m_{1,b} & p_{1,b}^* m_{2,b} \\ 0 & 0 & p_{2,b}^* m_{1,b} & p_{2,b}^* m_{2,b} \end{bmatrix}. \tag{3.28}$$

This matrix is non-Hermitian, which indicates the possible solutions of Eq. (3.26) are more complicated than those of a Hermitian matrix. A necessary condition for Eq. (3.26) to be satisfied is $\mathrm{Det}\,\mathbf{M} = 0$, and this can be shown through direct calculation to be automatically satisfied. A more involved calculation shows that of the four eigenvalues of the matrix, two of them are zero and two are non-zero.

Because the matrix $\mathbf{M}$ is non-Hermitian, it has distinct right and left eigenvectors and these represent distinct situations when Lissajous singularities will form. Thus,

$$\langle \mathbf{A}|\mathbf{M} = \langle \mathbf{0}| \tag{3.29}$$

and

$$\mathbf{M}|\mathbf{A}\rangle^{\dagger} = |\mathbf{0}\rangle \tag{3.30}$$

are two independent sufficiency conditions to satisfy Eq. (3.26).

The formulation of the bichromatic interference problem in the matrix form of Eq. (3.26) is the most significant finding of this paper. It provides a clear method for determining the conditions under which the incident bichromatic fields on the pinholes will produce Lissajous singularities. In the next section, we will delve into the exploration of the two categories of solutions to generate Lissajous singularities on the observation plane. Since both conditions are only sufficient, it is possible to find Lissajous singularities in some situations without necessarily satisfying these sufficiency criteria. We will provide an illustrative example of such a case as well.

## 3.4 Examples and discussions

We now look at the conditions of Eqs. (3.29) and (3.30) in turn. The condition $\langle \mathbf{A}|\mathbf{M} = \langle \mathbf{0}|$ represents the pair of equations

$$p^*_{1,a} e^{-\mathrm{i}k_a R_1} + p^*_{2,a} e^{-\mathbf{i}k_a R_2} = 0, \tag{3.31}$$

$$p^*_{1,b} e^{-\mathrm{i}k_b R_1} + p^*_{2,b} e^{-\mathrm{i}k_b R_2} = 0. \tag{3.32}$$

Because $R_1$ and $R_2$ represent quasi-independent distances, and $k_a$ and $k_b$ are very large at optical frequencies, $k_a R_1$ and $k_a R_2$ will produce every combination of phases over the observation plane. We write $k_a R_1$ as $\phi_1$, and $k_a R_2$ as $\phi_2$. Since $k_b = n k_a$, with $n = 2, 3, \ldots$, Eqs. (3.31) and (3.32) can be rewritten as

$$p^*_{1,a} e^{-\mathrm{i}\phi_1} + p^*_{2,a} e^{-\mathrm{i}\phi_2} = 0, \tag{3.33}$$

$$p^*_{1,b} e^{-\mathrm{i}n\phi_1} + p^*_{2,b} e^{-\mathrm{i}n\phi_2} = 0. \tag{3.34}$$

Thus

$$\begin{aligned} p_{1,a} &= A e^{-\mathrm{i}\phi_1}, \quad p_{2,a} = -A e^{-\mathrm{i}\phi_2}, \\ p_{1,b} &= B e^{-\mathrm{i}n\phi_1}, \quad p_{2,b} = -B e^{-\mathrm{i}n\phi_2}, \end{aligned} \tag{3.35}$$

with $A, B \in \mathbf{R}$. Figs. 3.2–3.4 illustrate solutions of Eq. (3.35) for different ratios of wavenumber and polarization states of the incident vector beams. We choose $m_{i,\beta} = (1 - |p_{i,\beta}|^2)^{1/2}$ in all these examples, with little loss of generality.

In Fig. 2(a), with $n = 2$, the intensity (solid red curve) exhibits periodic fluctuations and remains non-zero throughout. Lissajous singularities occur at the intersections of $\bar{S}_1 = 0$ and $\bar{S}_2 = 0$. In panel Fig. 2(b) it is seen that the orientation angle undergoes a $\pi/2$ jump across each singularity; an analogous $\pi/2$ change in orientation occurs when crossing a polarization singularity in a monochromatic field, regardless of whether

the type of generic polarization singularity is a lemon, star or monstar [2]. Along the $x$-axis, a recurring array of identical "crescent" Lissajous singularities (orange curves) forms, interspersed with non-singular Lissajous patterns of diverse shapes (cyan curves).

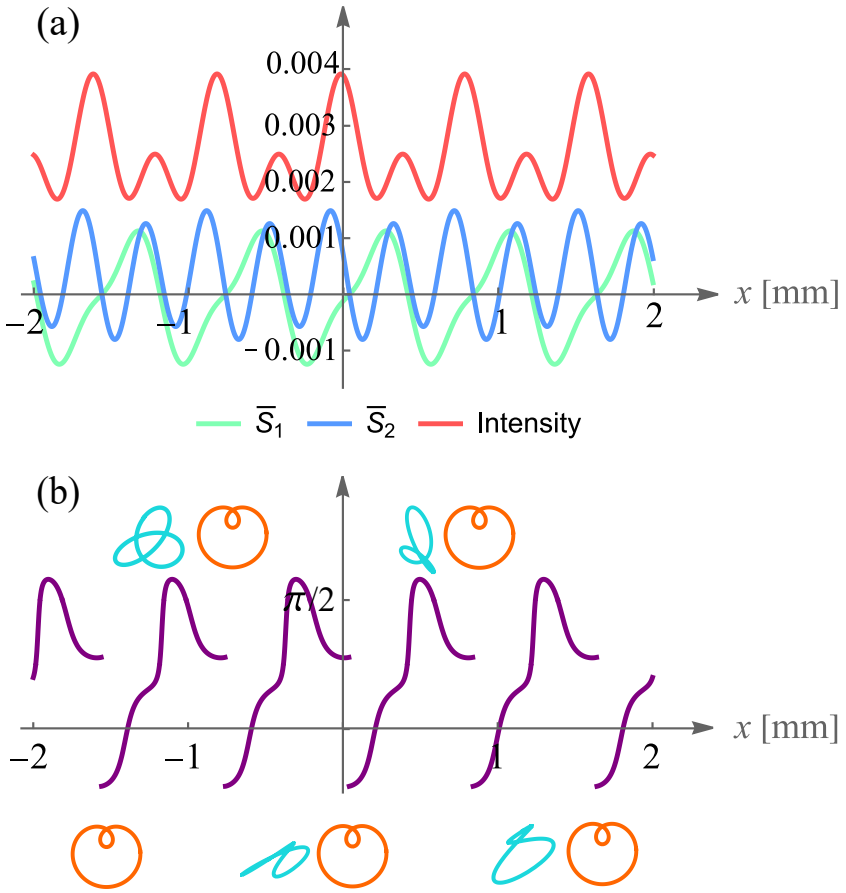


Figure 3.2: (a) Intensity [a.u.] (red) and the Stokes parameters $\bar{S}_1$ (green) and $\bar{S}_2$ (blue) along the $x$-axis on the observation screen. (b) Lissajous singularities (orange), non-singular Lissajous patterns (cyan) and the orientation angle $\psi$ (purple) along the $x$-axis on the observation screen. In this example $n = 2$, $\lambda_a = 800$ nm, $\lambda_b = 400$ nm. $p_{1,a} = (\sqrt{2}/3)\exp(\mathrm{i}3\pi/5)$, $p_{2,a} = -(\sqrt{2}/3)\exp(\mathrm{i}\pi/2)$, $p_{1,b} = (1/2)\exp(\mathrm{i}6\pi/5)$, and $p_{2,b} = (-1/2)\exp(\mathrm{i}\pi)$.

In Fig. 3.3, the frequency ratio $n$ is changed to 3, and we vary the choices of $p_{i,\beta}$. It is seen that the Lissajous singularities take on varied orientations compared to the identical orientations observed in Fig. 3.2. A video demonstrating the continuous evolution of Lissajous patterns along the $x$-axis can be found in Visualization 1.

In the previous examples, the change in polarization state was accompanied by

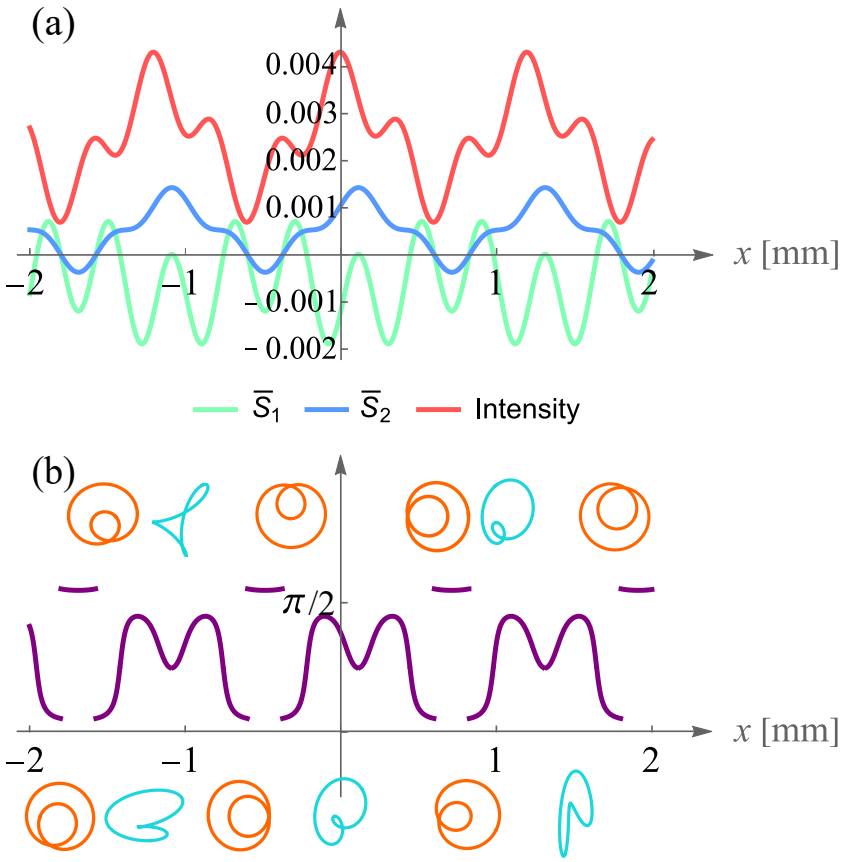


Figure 3.3: (a) Intensity [a.u.] (red) and the Stokes parameters $\bar{S}_1$ (green) and $\bar{S}_2$ (blue) along the $x$-axis on the observation screen. (b) Lissajous singularities (orange), non-singular Lissajous patterns (cyan) and the orientation angle $\psi$ (purple) along the $x$-axis on the observation screen. Here, $n = 3$, $\lambda_a = 1200$ nm, $\lambda_b = 400$ nm. $p_{1,a} = (\sqrt{2}/4)\exp(\mathrm{i}3\pi/2)$, $p_{2,a} = -(\sqrt{2}/4)\exp(\mathrm{i}\pi/8)$, $p_{1,b} = (1/2)\exp(\mathrm{i}9\pi/2)$, and $p_{2,b} = -(1/2)\exp(\mathrm{i}3\pi/8)$ (see Visualization 1).

significant changes in intensity. Fig. 3.4 shows that this need not be the case: for an appropriate choice of parameters, Lissajous patterns can manifest along the $x$-axis while the overall intensity remains effectively constant. In Fig. 4(a), the intensity is essentially constant over the range of interest; the intensity for each frequency is essentially constant as well. Though there is no observed pattern in intensity on the observation plane, periodic Lissajous singularities do appear at the intersections of $\bar{S}_1$ and $\bar{S}_2$ with the $x$-axis, as evidenced by the $\pi/2$ jumps in Fig. 4(b). In this case, Lissajous singularities are not only of crescent shape. Instead, trefoils and crescents appear alternately. This suggests a broader range of possible Lissajous singularity shapes on the observation screen. A video depicting the variation of Lissajous patterns along the $x$-axis in this scenario is included in Visualization 2.

We may also consider the second sufficiency condition, $\mathbf{M}|\mathbf{A}\rangle^\dagger = |\mathbf{0}\rangle$, which yields a pair of equations

$$m_{1,a}e^{\mathrm{i}k_aR_1} + m_{2,a}e^{\mathrm{i}k_aR_2} = 0, \tag{3.36}$$

$$m_{1,b}e^{\mathrm{i}k_bR_1} + m_{2,b}e^{\mathrm{i}k_bR_2} = 0. \tag{3.37}$$

Using a similar notation as for the previous case, we find that

$$\begin{aligned} m_{1,a} &= Ce^{-\mathrm{i}\phi_1}, \quad m_{2,a} = -Ce^{-\mathrm{i}\phi_2}, \\ m_{1,b} &= De^{-\mathrm{i}n\phi_1}, \quad m_{2,b} = -De^{-\mathrm{i}n\phi_2}, \end{aligned} \tag{3.38}$$

with $C, D \in \mathbf{R}$. Because $m_{i,\beta}$ are all real as we defined in Section 3, the phases $\phi_1$ and $\phi_2$ can only be multiples of $2\pi$. Thus Eqs. (3.38) reduce to

$$\begin{aligned} m_{1,a} &= C, \quad m_{2,a} = -C, \\ m_{1,b} &= D, \quad m_{2,b} = -D. \end{aligned} \tag{3.39}$$

Since $|p_{i,\beta}| = (1 - |m_{i,\beta}|^2)^{1/2}$, there is now no restriction on the phases of $p_{i,\beta}$, only

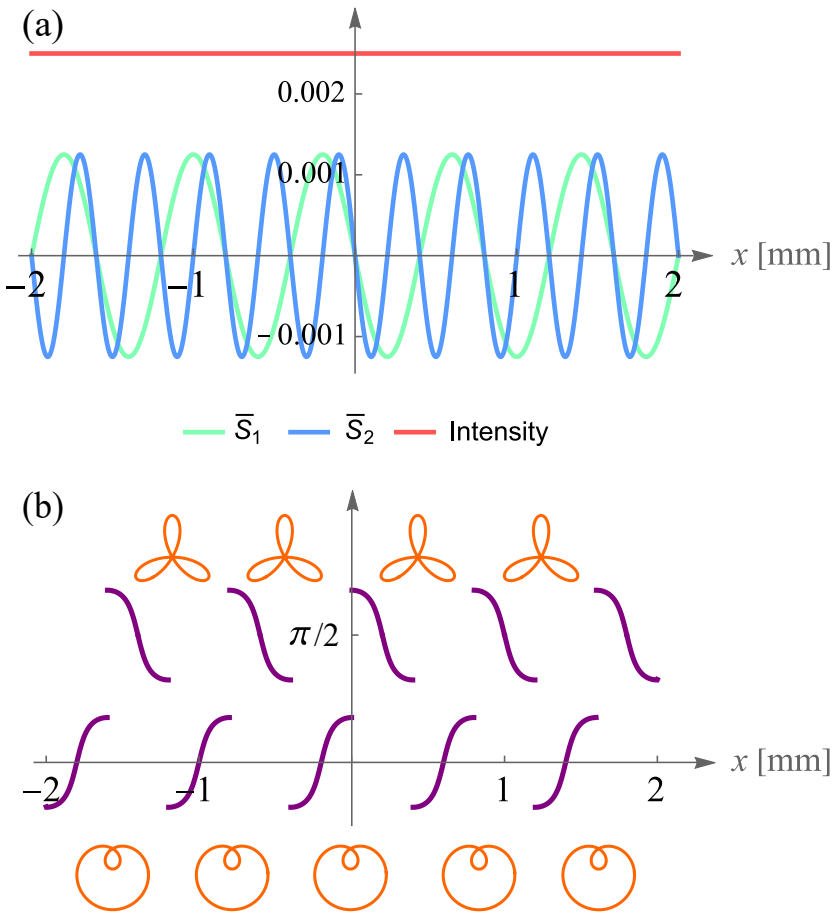


Figure 3.4: (a) Intensity [a.u.] (red) and the Stokes parameters $\bar{S}_1$ (green) and $\bar{S}_2$ (blue) along the $x$-axis on the observation screen. (b) Lissajous singularities (orange) and the orientation angle $\psi$ (purple) along the $x$-axis on the observation screen. Here, $n = 2$, $\lambda_a = 800$ nm, $\lambda_b = 400$ nm. $p_{1,a} = (\sqrt{2}/2)\exp(\mathrm{i}3\pi/2)$, $p_{2,a} = -(\sqrt{2}/2)\exp(\mathrm{i}3\pi/2)$, $p_{1,b} = (\sqrt{2}/2)\exp(\mathrm{i}3\pi)$, and $p_{2,b} = -(\sqrt{2}/2)\exp(\mathrm{i}3\pi)$ (see Visualization 2).

on their amplitude. Thus, in the following examples these four phases are randomly chosen.

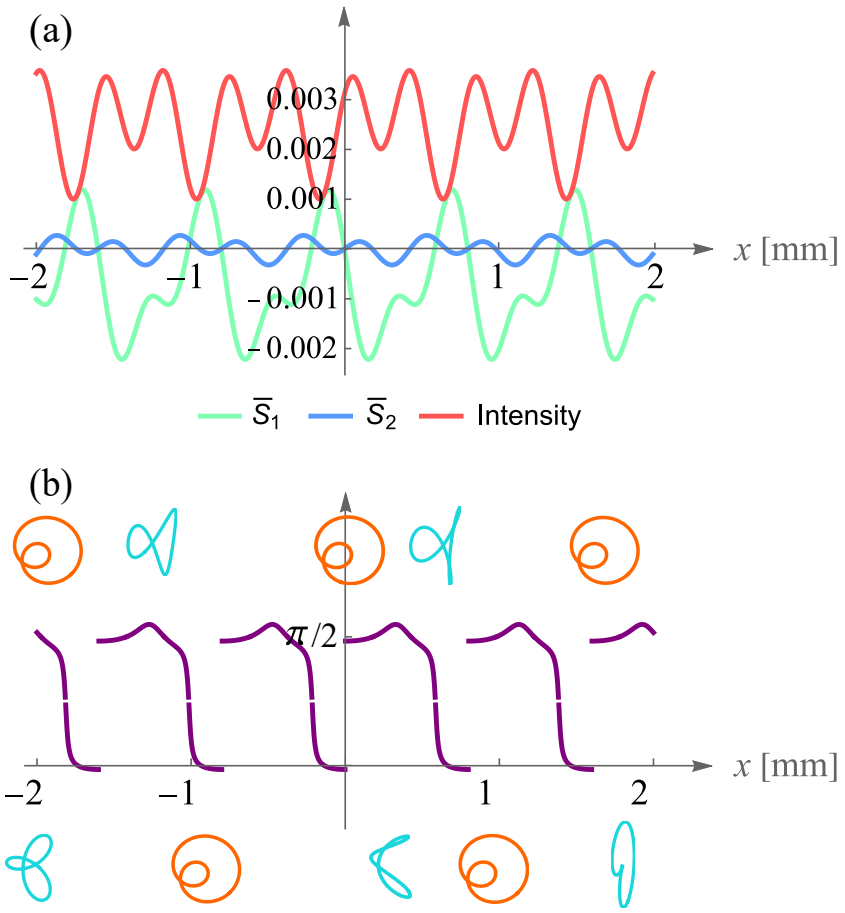


Figure 3.5: (a) Intensity [a.u.] (red) and the Stokes parameters $\bar{S}_1$ (green) and $\bar{S}_2$ (blue) along the $x$-axis on the observation screen. (b) Lissajous singularities (orange), non-singular Lissajous patterns (cyan) and the orientation angle $\psi$ (purple) along the $x$-axis on the observation screen. Here, $n = 2$, $\lambda_a = 800$ nm, $\lambda_b = 400$ nm. $m_{1,a} = \sqrt{2}/2, m_{2,a} = -\sqrt{2}/2, m_{1,b} = 1/3, m_{2,b} = -1/3, p_{1,a} = (\sqrt{2}/2)\exp(\mathrm{i}3\pi/5)$, $p_{2,a} = (\sqrt{2}/2)\exp(\mathrm{i}\pi/3)$, $p_{1,b} = (\sqrt{8}/3)\exp(\mathrm{i}2\pi/3)$, and $p_{2,b} = (\sqrt{8}/3)\exp(\mathrm{i}\pi/2)$.

In Figs. 3.5 and 3.6 two examples are presented for which Eqs. (3.39) are satisfied. Irrespective of the $p_{i,\beta}$, there is always a Lissajous singularity created at $x = 0$. This is because on the $z$-axis, $R_1 - R_2 = 0$ and hence the conditions (3.36) and (3.37) are automatically satisfied. Notice that in Fig. 3.5, with frequency ratio $n = 2$, again an array of identical Lissajous singularities is formed.

In Figs. 5(b) and 6(b), the blank spots in the continuous interval of the orientation

angle plots appear as $S_1 = 0$ while at those points $S_2$ does not equal 0. The mathematical software encounters challenges when calculating the Arctan function with an undefined value, resulting in gaps where we expect continuity.

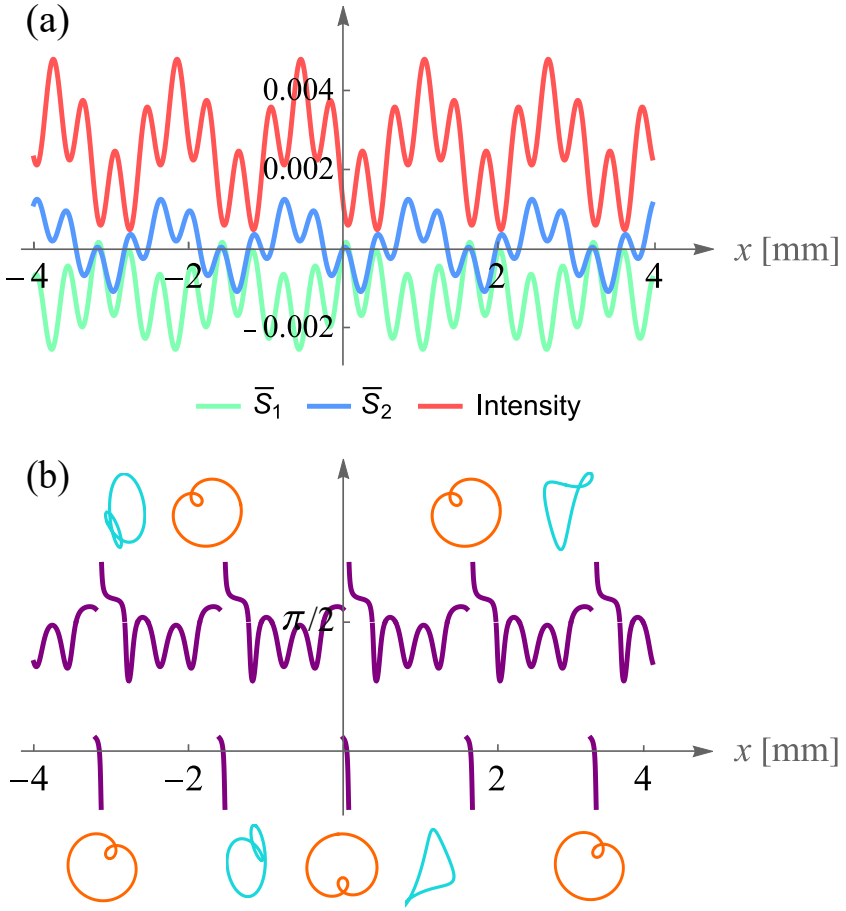


Figure 3.6: (a) Intensity [a.u.] (red) and the Stokes parameters $\bar{S}_1$ (green) and $\bar{S}_2$ (blue) along the $x$-axis on the observation screen. (b) Lissajous singularities (orange), non-singular Lissajous patterns (cyan) and the orientation angle $\psi$ (purple) along the $x$-axis on the observation screen. Here, $n = 4$, $\lambda_a = 1600$ nm, $\lambda_b = 400$ nm. $m_{1,a} = \sqrt{3}/5, m_{2,a} = -\sqrt{3}/5, m_{1,b} = 1/2, m_{2,b} = -1/2, p_{1,a} = (\sqrt{22}/5)\exp(\mathrm{i}3\pi/2)$, $p_{2,a} = (\sqrt{22}/5)\exp(\mathrm{i}\pi/8)$, $p_{1,b} = (\sqrt{3}/2)\exp(\mathrm{i}\pi)$, and $p_{2,b} = (\sqrt{3}/2)\exp(\mathrm{i}5\pi/3)$.

Because Eqs. (3.29) and (3.30) are only sufficient conditions, and not necessary ones, it should be possible to find cases where Lissajous singularities appear even though neither condition is satisfied. An example of this is shown in Fig. 3.7.

We set $m_{i,\beta} = (1-|p_{i,\beta}|^2)^{1/2}$, $n = 3$, $|p_{i,\beta}| = m_{i,\beta} = \sqrt{2}/2$, and the phases of $p_{i,\beta}$ are randomly chosen. Lissajous singularities appear with the same shape but different

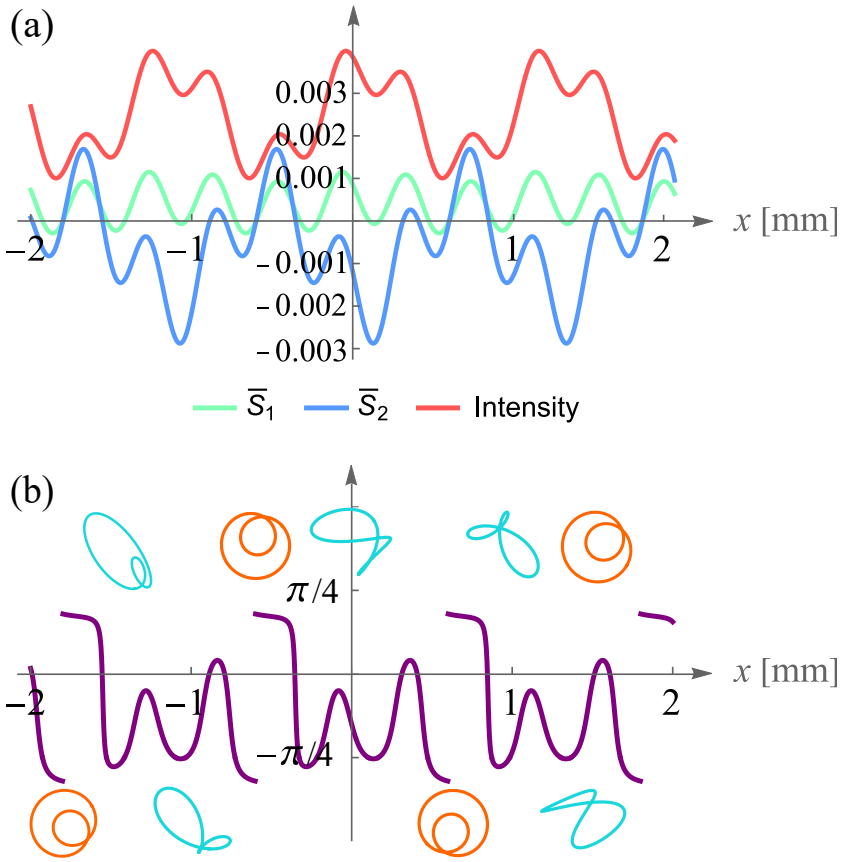


Figure 3.7: (a) Intensity [a.u.] (red) and the Stokes parameters $\bar{S}_1$ (green) and $\bar{S}_2$ (blue) along the $x$-axis on the observation screen. (b) Lissajous singularities (orange), non-singular Lissajous patterns (cyan) and the orientation angle $\psi$ (purple) along the $x$-axis on the observation screen. Here, $n = 3$, $\lambda_a = 1200$ nm, $\lambda_b = 400$ nm. $p_{1,a} = (\sqrt{2}/2)\exp(\mathrm{i}3\pi/5)$, $p_{2,a} = (\sqrt{2}/2)\exp(\mathrm{i}\pi/3)$, $p_{1,b} = (\sqrt{2}/2)\exp(\mathrm{i}4\pi/3)$, and $p_{2,b} = (\sqrt{2}/2)$.

orientations. This illustrates that the two independent conditions we derived are indeed sufficient, but not necessary.

## 3.5 Conclusions

We have examined the superposition of two bichromatic beams in Young's interference experiment, with the goal of finding conditions under which Lissajous singularities appear in interference. Two independent sufficiency conditions for the generation of Lissajous singularities were derived. Several examples, in which either of these conditions is satisfied, were presented, all showing a variety of Lissajous patterns, both singular and non-singular. Furthermore, it was demonstrated that, when neither of the two sufficiency conditions is satisfied, it is nevertheless possible to create singular polarization figures.

Though Lissajous singularities have been relatively unexplored to date, there is increasing interest in them, for example in studying unusual topological knots and Möbius strips in light waves [56]. The conditions presented in this paper should serve as a guide for future studies of such singularities.

# REFERENCES


[1] A. Forbes, M. De Oliveira, and M. R. Dennis, "Structured light," *Nature Photonics*, vol. 15, no. 4, pp. 253–262, 2021.

[2] G. Gbur, *Singular Optics*. Boca Raton: CRC Press, 2016.

[3] D. J. Richardson, J. M. Fini, and L. E. Nelson, "Space-division multiplexing in optical fibres," *Nature photonics*, vol. 7, no. 5, pp. 354–362, 2013.

[4] G. Gbur, "Partially coherent beam propagation in atmospheric turbulence," *JOSA A*, vol. 31, no. 9, pp. 2038–2045, 2014.

[5] G. Gbur, "Partially coherent vortex beams," in *Complex Light and Optical Forces XII*, vol. 10549, p. 1054903, SPIE, 2018.

[6] G. Gbur, T. D. Visser, and E. Wolf, "'hidden' singularities in partially coherent wavefields," *Journal of Optics A: Pure and Applied Optics*, vol. 6, no. 5, p. S239, 2004.

[7] Y. Gu and G. Gbur, "Topological reactions of optical correlation vortices," *Optics communications*, vol. 282, no. 5, pp. 709–716, 2009.

[8] W. Miao, Y. Zhang, and G. Gbur, "Partially coherent fractional fourier transform vortex beams," in *Frontiers in Optics + Laser Science 2022 (FIO, LS)*, p. JW4A.11, Optica Publishing Group, 2022.

[9] N. Rotenberg and L. Kuipers, "Mapping nanoscale light fields," *Nature Photonics*, vol. 8, no. 12, pp. 919–926, 2014.

[10] T. Bauer, S. Orlov, U. Peschel, P. Banzer, and G. Leuchs, "Nanointerferometric amplitude and phase reconstruction of tightly focused vector beams," *Nature Photonics*, vol. 8, no. 1, pp. 23–27, 2014.

[11] M. Soskin, S. V. Boriskina, Y. Chong, M. R. Dennis, and A. Desyatnikov, "Singular optics and topological photonics," *Journal of Optics*, vol. 19, p. 010401, dec 2016.

[12] D. A. Kessler and I. Freund, "Lissajous singularities," *Optics letters*, vol. 28, no. 2, pp. 111–113, 2003.

[13] G. Gbur and T. D. Visser, "Young's interference experiment: Past, present, and future," *Progress in Optics*, vol. 67, pp. 275–343, 2022.

[14] W. Miao, T. D. Visser, and G. Gbur, "Lissajous singularities in young's interference experiment," *Opt. Express*, vol. 32, pp. 813–824, Jan 2024.

[15] M. Soskin and M. Vasnetsov, "Singular optics," in *Progress in Optics* (E. Wolf, ed.), vol. 42, (Amsterdam), p. 219, Elsevier, 2001.

[16] M. Dennis, K. O'Holleran, and M. Padgett, "Singular optics: Optical vortices and polarization singularities," in *Progress in Optics* (E. Wolf, ed.), vol. 53, (Amsterdam), p. 293, Elsevier, 2009.

[17] G. Gbur, *Singular Optics*. CRC Press, 2017.

[18] P. Galajda and P. Ormos, "Complex micromachines produced and driven by light," in *Summaries of Papers Presented at the Lasers and Electro-Optics. CLEO'02. Technical Diges*, pp. 634–635, IEEE, 2002.

[19] K. Gahagan and G. J. Swartzlander, "Optical vortex trapping of particles," *Optics Letters*, vol. 21, no. 11, pp. 827–829, 1996.

[20] J. H. Lee, G. Foo, E. G. Johnson, and G. A. Swartzlander Jr, "Experimental verification of an optical vortex coronagraph," *Physical review letters*, vol. 97, no. 5, p. 053901, 2006.

[21] G. Gibson, J. Courtial, M. J. Padgett, M. Vasnetsov, V. Pas'ko, S. M. Barnett, and S. Franke-Arnold, "Free-space information transfer using light beams carrying orbital angular momentum," *Optics Express*, vol. 12, no. 22, pp. 5448–5456, 2004.

[22] J. Wang, J.-Y. Yang, I. Fazal, N. Ahmed, Y. Yan, H. Huang, Y. Ren, Y. Yue, S. Dolinar, M. Tur, and A. Willner, "Terabit free-space data transmission employing orbital angular momentum multiplexing," *Nature Photonics*, vol. 6, pp. 488–496, 2012.

[23] N. Simpson, K. Dholakia, L. Allen, and M. Padgett, "Mechanical equivalence of spin and orbital angular momentum of light: an optical spanner," *Optics letters*, vol. 22, no. 1, pp. 52–54, 1997.

[24] K. Ladavac and D. Grier, "Microoptomechanical pumps assembled and driven by holographic optical vortex arrays," *Opt. Exp.*, vol. 12, p. 1144, 2004.

[25] O. Korotkova and G. Gbur, "Chapter four - applications of optical coherence theory," in *A Tribute to Emil Wolf* (T. D. Visser, ed.), vol. 65 of *Progress in Optics*, pp. 43–104, Elsevier, 2020.

[26] R. H. Brown and R. Q. Twiss, "Lxxiv. a new type of interferometer for use in radio astronomy," *The London, Edinburgh, and Dublin Philosophical Magazine and Journal of Science*, vol. 45, no. 366, pp. 663–682, 1954.

[27] D. Klyshko, "Combine epr and two-slit experiments: Interference of advanced waves," *Physics Letters A*, vol. 132, no. 6-7, pp. 299–304, 1988.

[28] D. Huang, E. A. Swanson, C. P. Lin, J. S. Schuman, W. G. Stinson, W. Chang, M. R. Hee, T. Flotte, K. Gregory, C. A. Puliafito, *et al.*, "Optical coherence tomography," *science*, vol. 254, no. 5035, pp. 1178–1181, 1991.

[29] C. Ding, M. Koivurova, J. Turunen, and L. Pan, "Self-focusing of a partially coherent beam with circular coherence," *J. Opt. Soc. Am. A*, vol. 34, pp. 1441–1447, Aug 2017.

[30] O. Korotkova, L. Andrews, and R. Phillips, "Model for a partially coherent Gaussian beam in atmospheric turbulence with application in Lasercom," *Opt. Eng.*, vol. 43, p. 330, 2004.

[31] Y. Zhang, Y. Cai, and G. Gbur, "Partially coherent vortex beams of arbitrary radial order and a van cittert–zernike theorem for vortices," *Physical Review A*, vol. 101, no. 4, p. 043812, 2020.

[32] E. Wolf, "New theory of partial coherence in the space–frequency domain. part i: spectra and cross spectra of steady-state sources," *JOSA*, vol. 72, no. 3, pp. 343–351, 1982.

[33] H. M. Ozaktas and M. A. Kutay, "The fractional fourier transform," in *2001 European Control Conference (ECC)*, pp. 1477–1483, IEEE, 2001.

[34] A. W. Lohmann, "Image rotation, wigner rotation, and the fractional fourier transform," *JOSA A*, vol. 10, no. 10, pp. 2181–2186, 1993.

[35] V. Namias, "The fractional order Fourier transform and its application to quantum mechanics," *J. Inst. Maths Applics*, vol. 25, pp. 241–265, 1980.

[36] G. Gbur, *Singular Optics*. Boca Raton: CRC Press, 2016.

[37] I. Freund, "Bichromatic optical lissajous fields," *Optics Communications*, vol. 226, no. 1, pp. 351–376, 2003.

[38] H. Yan and B. Lü, "Dynamical evolution of lissajous singularities in free-space propagation," *Physics Letters A*, vol. 374, no. 35, pp. 3695–3700, 2010.

[39] A. Fleischer, O. Kfir, T. Diskin, P. Sidorenko, and O. Cohen, "Spin angular momentum and tunable polarization in high-harmonic generation," *Nature Photonics*, vol. 8, no. 7, pp. 543–549, 2014.

[40] E. Pisanty, G. J. Machado, V. Vicuña-Hernández, A. Picón, A. Celi, J. P. Torres, and M. Lewenstein, "Knotting fractional-order knots with the polarization state of light," *Nature Photonics*, vol. 13, no. 8, pp. 569–574, 2019.

[41] G. Gbur, "Singular optics," *The Optics Encyclopedia*, pp. 1–23, 2007.

[42] I. Freund, "Emergent polarization singularities," *Optics letters*, vol. 29, no. 6, pp. 539–541, 2004.

[43] W. Miao, Y. Zhang, and G. Gbur, "Deterministic vortices evolving from partially coherent fields," *Optica*, vol. 10, pp. 1173–1176, Sep 2023.

[44] K. Liu, Y. Cheng, Y. Gao, X. Li, Y. Qin, and H. Wang, "Super-resolution radar imaging based on experimental OAM beams," *Applied Physics Letters*, vol. 110, no. 16, 2017.

[45] G. Foo, D. M. Palacios, and G. A. Swartzlander, "Optical vortex coronagraph," *Optics Letters*, vol. 30, no. 24, pp. 3308–3310, 2005.

[46] J. Hajnal, "Singularities in the transverse fields of electromagnetic waves. II. observations on the electric field," *Proceedings of the Royal Society of London. A. Mathematical and Physical Sciences*, vol. 414, no. 1847, pp. 447–468, 1987.

[47] N. M. Garcia, I. De Erausquin, C. Edmiston, and V. Gruev, "Surface normal reconstruction using circularly polarized light," *Optics Express*, vol. 23, no. 11, pp. 14391–14406, 2015.

[48] T. Ishibashi, Z. Kuang, S. Yufune, T. Kawata, M. Oda, T. Tani, Y. Iimura, K. Sato, Y. Konishi, K. Akahane, *et al.*, "Magneto-optical imaging using polarization modulation method," *Journal of Applied Physics*, vol. 100, p. 093903, 2006.

[49] W. Liu, W. Liu, L. Shi, and Y. Kivshar, "Topological polarization singularities in metaphotonics," *Nanophotonics*, vol. 10, no. 5, pp. 1469–1486, 2021.

[50] I. Freund, "Bichromatic optical Lissajous fields," *Opt. Commun.*, vol. 226, pp. 351–376, 2003.

[51] W. Miao and G. Gbur, "Design of Lissajous beams," *Optics Letters*, vol. 47, no. 2, pp. 297–300, 2022.

[52] H. F. Schouten, G. Gbur, T. D. Visser, and E. Wolf, "Phase singularities of the coherence functions in Young's interference pattern," *Optics Letters*, vol. 28, pp. 968–970, Jun 2003.

[53] R. W. Schoonover and T. D. Visser, "Creating polarization singularities with an N-pinhole interferometer," *Physical Review A*, vol. 79, no. 4, p. 043809, 2009.

[54] J. D. Jackson, *Classical Electrodynamics*. New York: Wiley, 1999.

[55] M. Born and E. Wolf, *Principles of Optics*. Cambridge: Cambridge University Press, 1999.

[56] E. Pisanty, G. Machado, V. Vicuña-Hernández, A. Picòn, A. Celi, J. Torres, and M. Lewenstein, "Knotting fractional-order knots with the polarization state of light," *Nature Photonics*, vol. 13, pp. 569–574, 2019.

# APPENDIX A: SUPPLEMENTARY MATERIAL FOR "DESIGN OF LISSAJOUS BEAMS"

The following MATLAB code can be used to generate the Lissajous patterns of a Lissajous beam, as shown in the paper. The sample code here generates the Lissajous pattern in Fig.1(d).

```
vv=linspace(-2,2,7);
mypoints=length(vv);
xx=1;
[x,y]=meshgrid(vv,vv);% draw Lissajous patterns
gamma1=1;
gamma2=1;
beta1=1;%handedness of the vortex for frequency1
beta2=-1;%handedness of the vortex for frequency2
m1=1;%order of the vortex for frequency1
m2=1;%order of the vortex for frequency2

ax=sqrt(2)/4;
ay=sqrt(14)/4;
deltaA=pi/4;

bx=-sqrt(14)/4;
by=sqrt(2)/4;
deltaB=pi/4;
ex=ax.*(x+1i*beta1.*y)^m1+bx;%ex and ey are the
x and y components of the frequency1 field
```

```
21      ey=ay.*exp(1i*deltaA).*(x+1i*beta1.*y)^m1
22          +by.*exp(1i*deltaB);
23      fx=bx.*(x+1i*beta2.*y)^m2+ax;%fx and fy are the
24       x and y components of the frequency2 field
25      fy=by.*exp(1i*deltaB).*(x+1i*beta2.*y)^m2
26          +ay.*exp(1i*deltaA);
27      exr=real(ex);
28      exi=imag(ex);
29      eyr=real(ey);
30      eyi=imag(ey);
31      enorm=sqrt(exr.^2+exi.^2+eyr.^2+eyi.^2);
32      fxr=real(fx);
33      fxi=imag(fx);
34      fyr=real(fy);
35      fyi=imag(fy);
36      fnorm=sqrt(fxr.^2+fxi.^2+fyr.^2+fyi.^2);
37      totoalnorm=sqrt(fnorm.^2+enorm.^2);
38
39      a=1.5;
40      exnorm=ex./totoalnorm./(a*mypoints*.5);
41      eynorm=ey./totoalnorm./(a*mypoints*.5);
42      fxnorm=fx./totoalnorm./(a*mypoints*.5);
43      fynorm=fy./totoalnorm./(a*mypoints*.5);
44
45      tt=linspace(0,2.0*pi,60);
46      hold on;
47      axis('equal');
```

```
48      for ii=1:mypoints
49          for jj=1:mypoints
50           %draw the Lissajous pattern at each point
51           lissajousx=x(ii,jj)+real(exnorm(ii,jj).*
52           exp(-1i*tt)+xx*fxnorm(ii,jj).*exp(-2*1i*tt));
53           lissajousy=y(ii,jj)+real(eynorm(ii,jj).*
54           exp(-1i*tt)+xx*fynorm(ii,jj).*exp(-2*1i*tt));
55
56            plot(lissajousx,lissajousy);
57          end
58      end
```

# APPENDIX B: SUPPLEMENTARY MATERIAL FOR "DETERMINISTIC VORTICES EVOLVING FROM PARTIALLY COHERENT FIELDS"

In this supplemental material, we show a detailed derivation process of the cross-spectral density (CSD) along propagation, which is Eq. (3.18) in the original manuscript.

We begin with a Gaussian Schell-model vortex (GSMV) beam

$$W_0(\mathbf{r}_1, \mathbf{r}_2) = (x_1 - iy_1)(x_2 + iy_2)e^{-r_1^2/2\sigma^2}e^{-r_2^2/2\sigma^2}e^{-|\mathbf{r}_2-\mathbf{r}_1|^2/2\delta^2}. \tag{B.1}$$

First, we write the spectral degree of coherence in terms of its Fourier transform,

$$\mu_0(\mathbf{R}) = \int \tilde{\mu}_0(\mathbf{K})e^{i\mathbf{K}\cdot\mathbf{R}}d^2K, \tag{B.2}$$

where

$$\begin{aligned}\tilde{\mu}_0(\mathbf{K}) =& \frac{1}{(2\pi)^2}\int e^{-R^2/2\delta^2}e^{-i\mathbf{K}\cdot\mathbf{R}}d^2R, \\ =& \frac{\delta^2}{\pi}e^{-K^2\delta^2/2}.\end{aligned} \tag{B.3}$$

The cross-spectral density may then be expressed in the form,

$$W_0(\mathbf{r}_1, \mathbf{r}_2) = \int \tilde{\mu}_0(\mathbf{K})U_0^*(\mathbf{r}_1, \mathbf{K})U_0(\mathbf{r}_2, \mathbf{K})d^2K, \tag{B.4}$$

where $U_0(\mathbf{r}, \mathbf{K})$ represents a monochromatic tilted vortex beam,

$$U_0(\mathbf{r}, \mathbf{K}) = \frac{(x + iy)}{\sigma}e^{-r^2/2\sigma^2}e^{i\mathbf{K}\cdot\mathbf{r}}. \tag{B.5}$$

The 2-D FracFT for a tiled vortex beam can be defined as an integral transform

$$U_\alpha(\mathbf{r}, \mathbf{K}) = \int_{-\infty}^{\infty} \mathrm{F}_\alpha(\mathbf{r}, \mathbf{r}')U_0(\mathbf{r}', \mathbf{K})\, d^2r', \tag{B.6}$$

where $\mathrm{F}_\alpha(\mathbf{r}, \mathbf{r}')$ represents the 2-D FracFT kernel defined as

$$K_\alpha(\mathbf{r}, \mathbf{r}') = \frac{ie^{-i\alpha}}{2\pi\tau^2 \sin\alpha} e^{\frac{-i\cot\alpha r^2}{2\tau^2}} e^{\frac{i\mathbf{r}\cdot\mathbf{r}'}{\tau^2\sin\alpha}} e^{-\frac{i\cot\alpha r'^2}{2\tau^2}}. \tag{B.7}$$

Proper $\tau$ value needs to be chosen so that the beam width is invariant regardless of the choice of the FracFT order $\alpha$ in the source plane. To find the beam width, we integrate all the exponential terms of a normally incident Gaussian beam over the source plane,

$$\begin{aligned} I =& \int e^{\frac{-i\cot\alpha r^2}{2\tau^2}} e^{\frac{i\mathbf{r}\mathbf{r}'}{\tau^2\sin\alpha}} e^{\frac{-i\cot\alpha r'^2}{2\tau^2}} e^{\frac{-r'^2}{2\sigma^2}} d^2r' \\ =& e^{\frac{-i\cot\alpha r^2}{2\tau^2}} \int e^{-\left(\frac{i\cot\alpha}{2\tau^2}+\frac{1}{2\sigma^2}\right)r'^2} e^{\frac{i\mathbf{r}\mathbf{r}'}{\tau^2\sin\alpha}} d^2r'. \end{aligned} \tag{B.8}$$

We use the relation,

$$e^{-A(\mathbf{r}'-B)^2} = e^{-Ar'^2+2AB\mathbf{r}'-AB^2}, \tag{B.9}$$

For the above integral,

$$A = \frac{i\cot\alpha}{2\tau^2} + \frac{1}{2\sigma^2},\ B = \frac{i\mathbf{r}}{i\cos\alpha + \frac{\tau^2}{\sigma^2}\sin\alpha}, \tag{B.10}$$

and thus,

$$I = e^{\frac{-i\cot\alpha r^2}{2\tau^2}} e^{AB^2} \int e^{-A(\mathbf{r}'-B)^2} d^2r' = \frac{\pi}{A} e^{\frac{-i\cot\alpha r^2}{2\tau^2}} e^{AB^2}, \tag{B.11}$$

where

$$e^{AB^2} = e^{-\frac{\sigma^2}{2\tau^2\sin\alpha(i\cos\alpha\sigma^2+\tau^2\sin\alpha)}r^2}. \tag{B.12}$$

The beam width $\omega$ is found as

$$\begin{aligned}\omega &= \mathrm{Re}\left[-\frac{\sigma^2}{2\tau^2\sin\alpha(i\cos\alpha\sigma^2+\tau^2\sin\alpha)}-\frac{i\cot\alpha}{2\tau^2}\right]^{\frac{-1}{2}} \\ &= \frac{\sqrt{2}(\cos^2\alpha\sigma^4+\tau^4\sin^2\alpha)^{\frac{1}{2}}}{\sigma}.\end{aligned} \tag{B.13}$$

Beam width goes from $\sqrt{2}\sigma$ to $\frac{\sqrt{2}\tau^2}{\sigma}$, as the FracFT order $\alpha$ increases from 0 to $\pi/2$. So in order to keep all fractional beams sharing the same width, $\tau$ needs to be set as $\sigma$.

Then, the 2-D FracFT kernel is expressed as

$$\mathrm{F}_\alpha(\mathbf{r},\mathbf{r}') = \frac{ie^{-i\alpha}}{2\pi\sigma^2\sin\alpha}e^{\frac{-i\cot\alpha r^2}{2\sigma^2}}e^{\frac{i\mathbf{r}\cdot\mathbf{r}'}{\sigma^2\sin\alpha}}e^{-\frac{i\cot\alpha r'^2}{2\sigma^2}}. \tag{B.14}$$

After applying the FracFT to the tilted beams in the source plane, Fresnel diffraction can be used to propagate them to any desired distance. The field distribution along propagation is expressed as

$$U_\alpha(\mathbf{r},\mathbf{K},z) = \int \mathrm{G}(\mathbf{r},\mathbf{r}')U_\alpha(\mathbf{r}',\mathbf{K})d^2r', \tag{B.15}$$

Where $\mathbf{G}(\mathbf{r},\mathbf{r}')$ is the Fresnel diffraction kernel, given by

$$\mathrm{G}(\mathbf{r},\mathbf{r}') = \frac{e^{ikz}}{i\lambda z}e^{\frac{ik|\mathbf{r}-\mathbf{r}'|^2}{2z}}. \tag{B.16}$$

The 2-D FracFT and Fresnel diffraction integrals can be combined to write as

$$U_\alpha(\mathbf{r},\mathbf{K},z) = \int\int \mathrm{G}(\mathbf{r},\mathbf{r}')\mathrm{F}_\alpha(\mathbf{r}',\mathbf{r}'')U_0(\mathbf{r}'',\mathbf{K})d^2r''d^2r', \tag{B.17}$$

The integral over $r'$ can be calculated first to combine the FracFT and Fresnel kernel into the combined kernel

$$\begin{aligned} \mathrm{H}(\mathbf{r},\mathbf{r}'') &= \int \mathrm{G}(\mathbf{r},\mathbf{r}')\mathrm{K}_\alpha(\mathbf{r}',\mathbf{r}'')d^2r' \\ &= \frac{ie^{ikz}e^{-i\alpha}}{2\pi\beta^2} e^{\frac{ik}{2z}r^2} e^{\frac{-i\cot\alpha r''^2}{2\sigma^2}} e^{-\frac{i\gamma(\mathbf{r}''-\mathbf{r}/\gamma)^2}{2\beta^2}}, \end{aligned} \tag{B.18}$$

where $\beta^2 \equiv \sigma^2 \sin\alpha - \frac{z}{k}\cos\alpha$, $\gamma \equiv \frac{z}{k\sigma^2\sin\alpha}$.

Then the field distribution along propagation is obtained by the following integral

$$U_\alpha(\mathbf{r},\mathbf{K},z) = \int \mathrm{H}(\mathbf{r},\mathbf{r}'')U_0(\mathbf{r}'',\mathbf{K})d^2r''. \tag{B.19}$$

Substituting Eq. (B.5) and Eq. (B.18) and after lengthy calculations, Eq. (B.19) yields

$$U_\alpha(\mathbf{r},\mathbf{K},z) = \frac{-e^{ikz}e^{-i\alpha}}{4\beta^4A^2\sigma} e^{\frac{-(\sin\alpha+i\cos\alpha)}{4\beta^2A\sigma^2}r^2} e^{\frac{-\mathbf{K}\cdot\mathbf{r}}{2\beta^2A}} e^{\frac{-K^2}{4A}}[(x+k_x\beta^2)+i(y+K_y\beta^2)], \tag{B.20}$$

where $A \equiv \frac{i\tilde{\beta}^2}{2\beta^2\sigma^2} + \frac{1}{2\sigma^2}$, $\tilde{\beta}^2 \equiv \sigma^2\cos\alpha + \frac{z}{k}\sin\alpha$.

Then, the cross-spectral density along propagation can be obtained using a formula analogous to Eq. (B.4),

$$W_\alpha(\mathbf{r}_1,\mathbf{r}_2,z) = \int \tilde{\mu}_0(\mathbf{K})U^*_\alpha(\mathbf{r}_1,\mathbf{K},z)U_\alpha(\mathbf{r}_2,\mathbf{K},z)\,d^2K. \tag{B.21}$$

Substituting from Eq. (B.3) and Eq. (B.20) into the above integral yields

$$\begin{aligned} W_\alpha(\mathbf{r}_1,\mathbf{r}_2,z) = \frac{\delta^2}{16\beta^8|A|^4\sigma^2} & e^{-\frac{(\sin\alpha+i\cos\alpha)}{4\beta^2A\sigma^2}r_2^2} e^{-\frac{(\sin\alpha-i\cos\alpha)}{4\beta^2A^*\sigma^2}r_1^2} e^{\frac{(\mathbf{r}_1A+\mathbf{r}_2A^*)^2}{16\beta^4|A|^4\eta}} \\ & \left\{ \frac{1}{\eta^3}\Big[(\eta-\frac{1}{4A})(x_2+iy_2) - \frac{1}{4A^*}(x_1+iy_1)\Big]\cdot \right. \\ & \left. \Big[(\eta-\frac{1}{4A^*})(x_1-iy_1) - \frac{1}{4A}(x_2-iy_2)\Big] + \frac{\beta^4}{\eta^2}\right\}, \end{aligned} \tag{B.22}$$

where $\eta \equiv \frac{\delta^2}{2} + \frac{1}{4A} + \frac{1}{4A^*}$.

At the special distance $z_0$, the CSD reduces to

$$W_\alpha(\mathbf{r}_1, \mathbf{r}_2, z_0) = \frac{\delta^2}{16\beta^8|A|^4\sigma^2\eta} e^{\frac{(\mathbf{r}_2-\mathbf{r}_1)^2}{16\beta^4A^2\eta}} e^{-\frac{(\sin\alpha+i\cos\alpha)}{4\beta^2A\sigma^2}r_2^2} e^{-\frac{(\sin\alpha-i\cos\alpha)}{4\beta^2A^*\sigma^2}r_1^2} (x_1 - iy_1)(x_2 + iy_2), \tag{B.23}$$

which is in the form of a GSMV beam.